Global, Seasonal Cloud Variations from Satellite Radiance Measurements. Part I: Sensitivity of Analysis

WILLIAM B. ROSSOW, LEONID C. GARDER* AND ANDREW A. LACIS

NASA Goddard Space Flight Center, Institute for Space Studies, New York, New York

(Manuscript received 18 March 1988, in final form 4 November 1988)

ABSTRACT

Global, daily, visible and infrared radiance measurements from the NOAA-5 Scanning Radiometer (SR) are analyzed for the months of January, April, July and October 1977 to infer cloud and surface radiative properties. In this first paper in a three part series, the data and analysis method are described. A unique feature of the method is that it utilizes radiative transfer models that simulate the SR measurements using explicit parameters representing the properties of the surface, atmosphere, and clouds. The simulations also account for variations that depend on viewing geometry. The analysis combines several datasets so that the cloud contributions to the SR measurements can be isolated. The accuracy of all the results depends primarily on the proper separation of the total radiance distribution into those parts representing clear and cloudy scenes. Comparison of the surface properties retrieved from the clear scene radiances [see also Rossow et al. (1989)], sensitivity tests of the cloud detection algorithm, and comparisons of the resulting cloud amounts (see also Part II) provide an assessment of the accuracy of the method.

1. Introduction

A major uncertainty in the accurate determination of our climate's sensitivity to perturbation is the uncertainty in cloud-radiative feedback, or more accurately, cloud-radiative *feedbacks*. Though often described and envisioned as a singular positive or negative feedback term in the overall climate sensitivity, cloud-radiative interactions are actually very complex and involve many physical parameters, some of which are poorly measured, poorly understood, and/or are completely ignored in climate models. For example, cloud effects on the radiation field are produced by 1) cloud microphysical details: particle size, shape, phase, orientation, number density and the possible presence of aerosol contaminants; 2) cloud macrophysical properties: cloud cover, optical thickness, cloud top temperature, morphology, and geometric extent; 3) correlative context: surface albedo, atmospheric profiles of temperature, water vapor, aerosols, and ozone; and 4) time variability: solar zenith angle, cloud microphysical, macrophysical, and correlative context changes on diurnal, seasonal, and interannual time scales. Since the physical processes that operate to determine each cloud property can differ, it would be appropriate to associate a separate cloud-radiative feedback with each individual cloud parameter.

In principle, the radiative effects of changes in different cloud properties can be evaluated using conventional radiative transfer techniques, and indeed, the literature is full of many such studies. Thus, calculating the radiative effects of clouds is a tractable problem, at least to the extent that the different cloud physical properties, their atmospheric context, and time variability can be determined. However, climatological data characterizing all these aspects of clouds are lacking. On the other hand, the part of the cloud feedback loop associated with direct radiative effect (or indirect influence via atmospheric dynamics) on cloud physical properties is poorly understood and is an additional source of uncertainty in estimating the role of clouds in climate and in establishing the sign of cloud feedbacks on climate sensitivity.

The subtlety and significance of cloud feedbacks in climate has been amply demonstrated (e.g., Wang et al. 1981; Hansen et al. 1984), and this problem has been a primary focus of climate research in the last decade (GARP 1975, 1978; Rossow 1981; WCRP 1984). Study of this problem is necessarily indirect because there is no way to measure cloud and the consequent radiative changes during climate variations except by undertaking a multidecadal, global observation program. Progress can come, however, from the improvement and validation of the parameterized treatment of clouds and radiation in appropriate gen-

* Present affiliation: Columbia University, New York, New York.

Corresponding author address: Dr. William B. Rossow, NASA Goddard Space Flight Center, Institute for Space Studies, 2880 Broadway, New York, NY 10025.

eral circulation models (GCMs), which simulate cloud variations from mesoscales to planetary scales and over diurnal, synoptic, and seasonal time scales. Comparisons of clouds and radiation budgets from such models to detailed global observations that resolve these same scales can help to constrain and verify the parameterizations of the physical processes which affect cloud/radiation calculations and, thus, make the climate simulations of these models more believable. The International Satellite Cloud Climatology Project (ISCCP) and its associated research programs are designed to provide data and analysis results for such studies (Schiffer and Rossow 1983, 1985).

Some analyses of this problem infer cloud feedbacks on the seasonal cycle using simple, direct relationships between the satellite-measured spectral radiances and total fluxes (Cess 1976; Hartmann and Short 1980; Ohring and Clapp, 1980; Cess et al. 1982). These results are unsatisfactory because they ascribe all variations in the radiances and, thus, the total fluxes, to variations in cloud amount or cloud cover fraction. (Cess et al. 1982 also raise this point.) The fact that other cloud properties, as well as the surface and atmospheric properties, are changing seasonally is not taken into account. The neglect of the dependence of flux variations on changes in other cloud properties is equivalent to the assumption that all clouds have the same cloud top temperature, emissivity, and albedo at all times and locations. When these other cloud properties change as cloud cover varies, cloud radiative feedback on climate is considerably more complex (e.g., Wang et al. 1981; Stephens and Webster 1981; Somerville and Remer 1984).

Wang et al. (1981) illustrate this point by showing that the same climate model with more than one cloud property allowed to change can exhibit cloud-radiative feedbacks of opposite sign for different perturbations of the model climate, even though these perturbations have about the same amplitude. Thus, variation of more than one cloud property at a time makes the feedback a function of the space and time *structure* of the climate perturbation, in addition to its amplitude; hence a more detailed understanding of the distribution and variation of cloud properties is needed.

The alternative of calculating cloud radiative feedback using available cloud climatologies (London 1957; Telegadas and London 1954; Van Loon 1972; Schutz and Gates 1971a,b; Berlyand and Strokina 1980; see also Hughes 1984; Warren et al. 1985) is also unsatisfactory because the information provided on the geographical distribution of clouds or cloud radiative properties is incomplete. These climatologies do provide statistics on cloud morphological types, cloud base height (above local topography), and cloud cover fraction (variously defined), but do not provide information on cloud albedo or cloud top and base temperatures. Also, the coverage of the ocean-covered parts of the earth, especially in the Southern Hemisphere, is very poor or incomplete. Although improved coverage may be attainable in cloud climatologies based on ground-based observations, a cloud climatology with uniform global coverage is most readily obtained from satellite-based measurements.

Many cloud analysis techniques for satellite data have been proposed and studied (see Table 1; also Rossow et al. 1985). Although all of these methods are called "cloud algorithms," they are actually designed for many distinct purposes and cannot be used interchangeably without alterations. Obtaining a global cloud climatology that is suitable for study of cloud-radiation interactions requires analysis methods that not only detect the presence of clouds in satellite data, but also infer at least the most important optical properties from the radiance measurements. Many studies in the literature present methods that stop with the identification of clouds, without providing any quantitative information about their properties; others go on to obtain one or more specific cloud properties, though generally only cloud amount (variously defined) is discussed.

Of the methods listed in Table 1, only Reynolds and Vonder Haar (1977), Rossow et al. (1983), Minnis and Harrison (1984a,b,c), and Arking and Childs (1985) retrieve a "radiatively complete" set of quantities, i.e., one that represents the effect of clouds on both the solar and thermal-infrared parts of the spectrum. Only the method of Minnis and Harrison (1984a) has been used for a systematic study of the diurnal variations of clouds (Minnis and Harrison 1984b,c), but these results are limited to lower latitudes for one longitude sector and cover only 1 month. Only the method of Stowe (1984) has been used to obtain a global climatology, (cf. Hwang et al. 1988; Stowe et al. 1988, 1989) but this analysis does not provide adequate information about diurnal variations of clouds nor does it contain any measure of the optical properties of clouds at solar wavelengths. The USAF three-dimensional (3-D) nephanalysis also produces global cloud cover and altitude statistics, but no information on cloud solar reflectance or temperature is provided. Moreover, construction of climatological results from the 3-D Nephanalysis data is made difficult by frequent changes in data sources and data processing methodology (Fye 1978). A 1 yr climatology of global cloud cover from the 3-D nephanalysis has been studied by Hughes and Henderson-Sellers (1985) (see also Henderson-Sellers and Hughes 1985; Henderson-Sellers 1986).

For the past 8 yr, we have been investigating a specific quantitative approach to the determination of cloud-radiative feedback that combines the information in several datasets into a single consistent analysis. The strategy has three steps (see also, Minnis and Harrison 1984a,b,c):

TABLE 1. Historical summary of cloud algorithms

Method	Reference
VIS threshold[a], specified but selected manually	Arking (1964)
Manual nephanalysis[b]	Young (1967)
VIS/IR 2-D histogram, qualitative analysis[c]	Vonder Haar (1970)
VIS threshold, selected with VIS histogram analysis	Stamm and Vonder Haar (1970)
VIS scaling[d]	Miller and Feddes (1971)
VIS/IR threshold selected with histogram analysis	Shenk and Salomonson (1972b)
IR threshold with ancillary data for clear sky[e]	Koffler et al. (1973)
IR scaling modified by VIS analysis (manual selection)	Shenk and Curran (1973)
IR temperature sounding	Chahine (1974, 1977, 1982)
IR temperature sounding	Chahine et al. (1977)
Four-channel scene classification with IR slicing[f], uses ancillary data	Shenk et al. (1976)
IR temperature sounding	McCleese and Wilson (1976)
VIS/IR scaling, min/max composite for clear sky[g]	Reynolds and Vonder Haar (1977)
VIS threshold plus spatial "texture" analysis[h]	Harris and Barrett (1978)
VIS scaling	Curran et al. (1978)
Specified VIS threshold, microwave threshold and threshold with ancillary clear sky data	Smith et al. (1979)
VIS/IR threshold plus spatial "texture" analysis	Bunting and Fournier (1980)
VIS/IR scaling using time compositing with ancillary data for clear sky	Rossow (1981); Rossow et al. (1983)
IR spatial coherence, assumed clear cluster	Coakley and Bretherton (1982)
VIS/IR 2-D histogram "cluster" analysis, assumed clear cluster[e]	Desbois et al. (1982)
VIS/IR 2-D histogram "cluster" analysis, assumed clear cluster	Simmer et al. (1982)
Same as Smith et al. (1979) with thermal IR spatial variance	McMillin and Dean (1982)
VIS/IR 2-D histogram "cluster" analysis, VIS threshold to determine clear cluster	Phulpin et al. (1983)
IR threshold using ancillary data	Stowe (1984)
Hybrid histogram analysis with VIS/IR threshold, time compositing for clear sky	Minnis and Harrison (1984a)
IR temperature sounding (cf. Smith et al. 1979)	Susskind et al. (1984), Susskind et al. (1978)
VIS/IR 2-D histogram time analysis	Desbois and Séze (1984)
IR spatial coherence with IR threshold and time/space compositing for clear sky cluster	Coakley and Baldwin (1984)
Thermal IR spectral discrimination[j]	Llewellyn-Jones et al. (1984)
IR temperature sounding	Yeh (1984); Yet et al. (1985)
VIS/IR 2-D histogram "maximal cluster"[i] analysis, min/max for clear sky[i]	Arking and Childs (1985)
VIS threshold with VIS/IR scaling or 2-D histogram analysis	England and Hunt (1985)
VIS/IR threshold, specified	Saunders (1985)
Partly dynamic VIS/IR threshold	Chou et al. (1986)
Combination of several methods, multispectral	Saunders (1986); Saunders and Kriebel (1988)
Thermal IR multispectral discrimination	d'Entremont (1986)
Thermal IR spectral discrimination and threshold	Inoue (1987)
Dynamic IR threshold	Coakley (1987)
Combination of several methods, multispectral	Minnis et al. (1987)
Combination of several methods, plus time minimum of VIS spatial variance	Gutman et al. (1987)
Thermal IR spectral discrimination and threshold[j]	Yamanouchi et al. (1987)
VIS spectral discrimination and IR threshold, min/max[j]	Sakellariou and Leighton (1988)
Thermal IR threshold with ancillary clear sky data plus UV radiance scaling	Stowe et al. (1988)

[a] The threshold is the radiance value that divides the data into clear and cloudy categories; it is either a selected value or a small incremental difference from a deduced clear sky radiance.

[b] Manual nephanalysis is a procedure of visual inspection of photographs; it is actually equivalent to a threshold technique but may involve some pattern recognition aspects.

[c] One- and two-dimensional histograms refer to frequency histograms of radiance values usually collected over small regions.

[d] Scaling methods assume that cloud amount is directly proportional to the radiance values.

[e] Some methods specify the clear sky radiance values from other data sources and not from the satellite measurements.

[f] A slicing method divides the dataset into groups by sorting the radiance values into several ranges. For example, in the IR this is equivalent (approximately) to dividing regions by height.

[g] A min/max composite is constructed by examining a time record of radiances at each location to find the extremum (minimum VIS or maximum IR); this extreme value is assumed to represent clear sky conditions.

[h] Texture analysis searches for distinctive spatial variations of the radiances that are assumed to be associated with clouds.

[i] In the analysis of radiance histograms, some techniques look for concentrations of data, referred to as clusters. In the Arking and Childs method, the cloud amount in each image pixel is modified to minimize the size of these clusters.

[j] Spectral discrimination refers to use of two or more spectral channels to identify cloudy or clear conditions from differing wavelength dependences.

1) obtain a climatology of cloud radiative properties from analysis of satellite-measured narrowband radiances;

2) calculate a climatology of the total planetary and surface radiation balances from the cloud climatology; and

3) compare the cloud and radiation budget climatologies to those from a climate GCM.

The first step is to retrieve cloud radiative properties from satellite-measured *spectral radiances* with a self-consistent radiative transfer model that is specifically designed to simulate the satellite measurements by explicitly accounting for the separate effects of the earth's surface, atmosphere, and clouds. The explicit separation of the contributions from the atmosphere, surface, and clouds in the radiative model allows for the diagnosis of their separate contributions to changes in both the solar and thermal infrared radiances and to changes in the radiation budget. This approach requires correlative information about atmospheric and surface properties to isolate the cloud properties from cloudy scene measurements. However, since the data analysis must separate cloudy and clear scenes as the first step, the satellite data for clear scenes can be used to determine the surface optical properties in a self-consistent manner. Other data are used to specify the atmospheric state and to aid the separation of the satellite measurements into cloudy and clear portions. This use of correlative data is preferred since, of the three elements, the most complete information from other sources is available for the atmosphere.

In the second step, the parameter set describing the surface, atmosphere, and clouds is used in related radiative transfer models to calculate *spectrally integrated fluxes* and to investigate cloud-radiative feedbacks. This requires that the radiative model parameters be defined so that they can be used to calculate the effect of clouds both on satellite-measured, narrowband radiances and on total radiative fluxes, separately from and together with the atmospheric and surface effects. This calculation is also aided by additional datasets that specify parameters not obtained in the first step of the analysis.

The third step is to compare the cloud properties and the radiative fluxes, obtained from the combined analysis of the several datasets, to those produced by a climate model. Because the comparison includes both input and output parameters for the parameterizations that produce clouds and radiation in the climate model, diagnosis of any differences can be more specific. For example, if the upward infrared flux at the top of the model atmosphere differs from that in the data, the contribution of the clouds can be separated from that of the surface and atmosphere. The questions raised by such a comparison will define further data analyses to improve the climate model validation.

The analysis concept outlined above involves many steps, some of which are not well understood; hence, results at each step in the analysis must also be verified by additional data comparisons. This validation effort leads to improved radiative models both for remote sensing and for climate simulation applications. The validation strategy concerns the fidelity of five key factors:

1) the separation of the satellite measurements into cloudy and clear scenes in step 1;
2) the radiative model representation of the angular variation of satellite-measured narrowband radiances in step 1;
3) the radiative model parameterization of the space and time variations in cloud, surface and atmospheric optical properties in steps 1 and 2;
4) the radiative model representation of the spectral dependence of radiation in step 2; and
5) the radiative model representation of the radiation balance at the top of the atmosphere, within the atmosphere, and at the surface in step 2.

This paper (Part I) and two companions [(Rossow et al. 1989; hereafter referred to as Ro89) and Part II (Rossow et al. 1990; hereafter referred to as Part II)] report on progress made in understanding and validating some aspects of the analysis concept discussed above. Part I describes the data and methodology used for step 1 (sections 2 and 3). Section 4 reviews the tests used to determine the sensitivity of the cloud detection and radiative model analysis and compares the results of this cloud detection method to other analyses. Section 5 in Part I summarizes the estimated uncertainties of the analysis method.

We have carried the analysis of a limited dataset through all three steps to identify the key uncertainties and problems that need further study; however, we have not completed a validation of all the aspects mentioned above. The focus of our validation efforts thus far has been the determination of the accuracy of the cloud detection step; hence, we have not pursued all issues to the same degree. For example, a key aspect of the validation of the cloud detection is the accuracy of the clear sky radiances obtained, which depend primarily on the surface properties (see section 3 and Rossow et al. 1985). Thus, we provide validation of these surface properties sufficient to determine the accuracy of the cloud detection, but not necessarily sufficient for the study of the surface, itself. The results of this validation are summarized here. However, since these surface properties are important determinants of the surface radiation balance and are also of interest to other remote sensing investigations; a more detailed discussion of these surface results is presented in Ro89.

A complete validation of the angular and spectral variation of radiation in our radiative models is not possible with the dataset we have and must await the production of more comprehensive datasets by ISCCP, FIRE (First ISCCP Regional Experiment), and ERBE (Earth Radiation Budget Experiment). We report the results of sensitivity tests herein that address some aspects of the fidelity of the radiative model parameterizations. A crucial factor in the model representation of the radiative effects of clouds is the treatment of the complex spatial and temporal variability of cloudiness; hence, a key objective for this early cloud analysis is

the characterization of the scales and magnitudes of this variability. In Part II we present the results of our analysis, which describe the cloud variations on seasonal time scales for length scales from 100 km to planetary scale. These results complement those of Minnis and Harrison (1984a,b,c), who examine cloud variations on diurnal time scales for similar spatial scales. We also examine in Part II the radiation balance and cloud-radiative feedbacks inferred from the cloud results and compare them to those obtained by a climate GCM. The comparison serves to highlight the information content and accuracy of cloud and radiation budget datasets required to validate climate model parameterizations.

2. Data

The objective of this study is to investigate the global and seasonal variations of cloud properties and their effect on the radiation balance. The only readily available source of uniform global observations is from polar orbiting satellites. Data from sun-synchronous polar orbiters cannot provide proper coverage of the diurnal variations of clouds; however, the nearly constant time of overflight of these satellites does provide a measure of the seasonal variations for a particular time of day. To infer both solar and infrared optical properties of clouds and to characterize cloud structure for the primary atmospheric scales (mesoscale and larger), we utilize imaging data, which measures both solar reflectance and infrared emission for regions $\approx 8 \times 8$ km, rather than the coarser resolution thermal sounding instruments. We also select data from narrowband imaging instruments, rather than broadband instruments, to maximize the sensitivity to clouds. Retrieval of both solar and thermal cloud properties limits our analysis to the "illuminated" portions of the globe; hence, our results are based on daily measurements at each location and the seasonal coverage of the polar regions does not include the winter season. We selected the first year, 1977, in which the space and time coverage of the imager data was most nearly complete and for which radiation budget data (NIMBUS-6) were available. (We began this investigation in 1979.)

Extraction of cloud properties from the satellite-measured radiances requires the removal of the radiative effects contributed by the atmosphere and surface and radiative transfer models to compute the cloud effects. Since the only available global datasets for the atmosphere and surface do not specify their radiance effects directly, we must also have radiative transfer models that link the surface reflectance, surface temperature, atmospheric composition (including water vapor distribution), and atmospheric thermal structure to satellite measurements. The particular datasets described below were selected because they are global in extent and have the highest possible spatial and temporal resolutions. Since very few global datasets were available to choose from, however, our analysis procedures must combine datasets with differing spatial and temporal resolutions in such a way as to provide a self-consistent interpretation of the radiances.

A minimum set of parameters needed to model satellite visible and infrared radiances at one specific time and place consists of the following: (i) for the surface: visible reflectance (RS) (we assume isotropic reflectance except for water surfaces) and temperature (TS) (we assume an emissivity of 1), (ii) for the atmosphere:[1] ozone column abundance (O3), water vapor profile [e.g., relative humidity as a function of pressure, RH(p)], and temperature profile [$T(p)$], and (iii) for clouds: the optical thickness (TAU), referenced to visible wavelengths,[2] and top temperature (TC). (We assume conservative scattering at 0.6 μm, and no scattering at 11 μm). The cloud top temperature can also be related to a cloud top pressure (PC) or height above mean sea level (ZC) using the atmospheric temperature profile. In order to retrieve the two basic cloud properties, TAU and TC, we must specify the other quantities at each point, every day. For geographic regions that are larger than the instrument field of view (FOV), the cloud cover, CC, is defined by the number of cloudy image pixels (representing one radiometer field of view, FOV) in that region (see section 3).

a. Satellite radiances

The basic satellite radiance data are from the scanning radiometer (SR) on the NOAA-5, polar orbiting, operational weather satellite from January, April, July, and October 1977. All digital data are obtained from NOAA NESDIS in "polar stereo mosaic" format (NOAA 1977a; Fortuna and Hambrick 1974). The

[1] Climatological aerosol amounts could be included but are not in this analysis. The total optical thickness of aerosols is only about 0.1–0.3 (e.g., Toon and Pollack 1976), but most of the effect is caused by aerosols near the surface and below the clouds. Since the surface reflectances are retrieved from the same data using the same assumption, the average aerosol effect is included as part of the surface effect.

[2] Values of TAU are calculated at 0.6 μm wavelength, approximately the NOAA 5 SR band-center. The mean particle extinction cross section at 0.6 μm is obtained from full Mie calculations for a distribution of water spheres, with an effective radius of 10 μm and an effective size dispersion of 0.15 (see footnote on p. 28 and Hansen and Travis 1974), using the spectral dependence of the indices of refraction of water (Hale and Querry 1973). This approach permits TAU to be calculated for other wavelengths and to be converted to cloud particle column number density and liquid water content. The column number density is $N = \mathrm{TAU}/QG$, where $Q = 2.119$ is the normalized Mie extinction cross section at 0.6 μm and $G = 1.03 \times 10^{-4}$ cm^2 is the mean geometric cross section per particle. The liquid water content is given by $\mathrm{LWC} = \frac{4}{3}(A)(\mathrm{TAU}/Q)$, where $A = 10^{-3}$ cm is the effective particle radius.

SR measures visible (VIS) and infrared (IR) radiances over the wavelength ranges of 0.52–0.72 μm and 10.5–12.5 μm (Fig. 1) with a spatial resolution at the subsatellite point of 4 and 8 km, respectively. We ignore the difference in spatial resolution between the two channels, explicitly assuming (as in the radiative model) that the cloud properties are uniform over an 8 km × 8 km area. The satellite is in a sun-synchronous orbit allowing one daylight (morning) view of each location on earth, except at high latitudes where orbits overlap. Data volume is reduced, operationally, by limiting observations to satellite zenith angles $\leq 60°$ and sampling the data to provide one VIS and IR measurement every 15–25 km. For regions viewed more than once per day, only the last observation entered into the dataset is saved in the polar stereo mosaic format; operational processing irregularities make the actual times of observations at high latitudes much more variable than intended.

Visible radiances are reported as coded intensity values divided by the cosine of the solar zenith angle. Laboratory calibration of the instrument gives a relation between the coded intensity value (counts) and intensity in units of ft-lamberts (fL) (1 count = 40 fL), a photometric engineering unit which represents the brightness measured by a standard "human eye" radiometer with the spectral response function shown in Fig. 1a. Thus, the count value on the data tape, CT, gives a radiance, L^*,

$$L^* = (L^*_{\text{cal}}/\text{CT}_{\max}) \times \text{CT}$$

$$L^*_{\text{cal}} = s^0 \int s(\lambda)\phi_e(\lambda)d\lambda \quad (\text{fL})$$

where $s(\lambda)$ is the normalized spectrum of the calibration light source, s^0 the maximum intensity of the calibration source, and $\phi_e(\lambda)$ the normalized spectral re-

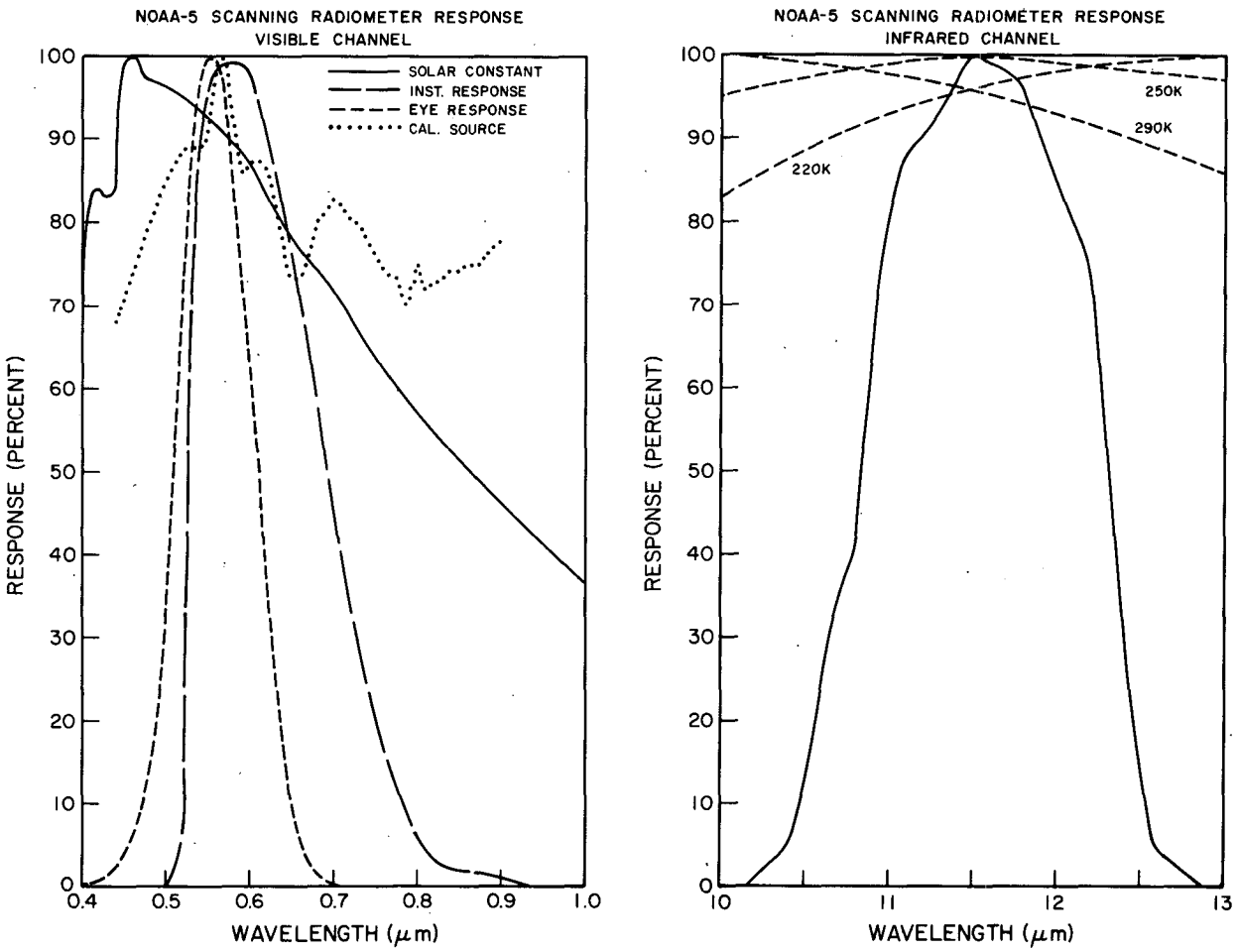

FIG. 1. Normalized spectral response functions for the NOAA-5 SR channels: (a) VIS and (b) IR. Also shown with the VIS response function are a normalized solar spectrum, calibration source spectrum, and the standard photometric function, representing the response of the human eye. Shown with the IR response function are normalized Planck spectra for three temperatures.

sponse of the "human eye" radiometer (Fig. 1a). The radiance measured by the instrument, when observing the calibration source, is given by

$$L_{cal} = s^0 \int s(\lambda)\phi(\lambda)d\lambda \quad (\mathrm{W\ m^{-2}\ sr^{-1}})$$

where $\phi(\lambda)$ is the normalized SR spectral response (Fig. 1a). Thus, the counts are converted to SI radiance units using the ratio,

$$L_{cal}/L^*_{cal} = 7.70 \times 10^{-3} \quad (\mathrm{W\ m^{-2}\ sr^{-1}})(\mathrm{fL})^{-1}.$$

Correcting for the spectral differences between the calibration source and the sun requires multiplying the data values by the ratio, $L/L^* = 1.0538$, where

$$L^* = s^0 \int s(\lambda)\phi(\lambda)d\lambda$$

$$L = S_0 \int S(\lambda)\phi(\lambda)d\lambda.$$

Here, $S(\lambda)$ is the normalized solar spectrum (Fig. 1a), and S_0 is the total solar intensity. The solar constant (1368 W m^{-2}) multiplied by the instrument response is 260.02 W m^{-2} (or 82.77 W m^{-2} sr^{-1}). Thus, CT is converted to radiance by

$$L = (L/L^*)(L_{cal}/L^*_{cal})(L^*_{cal}/\mathrm{CT}_{max})(\mathrm{CT}). \quad (1)$$

Laboratory calibration results have been reported only for the NOAA-2 SR (Conlan 1973) and verified using an earth target (Jacobowitz and Gruber 1975); but comparison of results over the whole NOAA series suggests similar calibrations within 5%–10% (Gruber 1977). We have also verified the calibration to within 10%–15% by comparison of the satellite-measured surface reflectances for ocean and land to literature values (see Matthews and Rossow 1987).

Laboratory measurements suggest a noise level in the VIS channel of SR of about 2% (A. Gruber, personal communication); after launch, some mirror scan motor noise was also apparent in the VIS data (Conlan 1973). The sampling procedure used by NOAA in processing the data, together with errors in navigation, leads to a nearly random spatial distribution of noise from the scan motor and other sources. To verify the magnitude of the VIS channel noise, we accumulated one month of surface reflectance values over the whole ocean, which represents (approximately) a dark, uniform surface. Although the effects of variable viewing geometry, of variable wind roughening of the surface, and of variations of suspended particulates contribute to some variations of the derived reflectance of the ocean, these effects generally increase the reflectance. The distribution of observed surface reflectances has a large peak at about 2%–4%, consistent with the reflectance value predicted for Fresnel reflection from a flat water surface, and a distribution width below the mode of about 2%–3%, consistent with the interpretation that the noise level is no more than about 2%.

Infrared radiance (Fig. 1b) measurements are calibrated by an on-board black-body source with known temperature. The estimated accuracy of this calibration for the NOAA-5 SR is 2 K. Measurements are reported as brightness temperatures with an empirical correction (applied by NOAA) for water vapor absorption that is a function of satellite zenith angle and temperature (Conlan 1973; Gruber 1977). The temperature dependence of the correction approximates the variation of the attenuation due to variations in water amount in a way that is equivalent to assuming that the relative humidity profile is constant. We remove the empirical correction to calculate a more detailed water vapor correction consistent with our radiative model and temperature/humidity data.

A complete description of the viewing geometry (described by solar and satellite zenith angles and the relative azimuth angle) is needed to compare measured and modeled radiances. Obtaining this information requires calculating the location of the satellite when it views each location on the surface of earth—the inverse of the procedure used to map the data into the polar stereographic mosaics (Ruff and Gruber 1975). This calculation requires assignment of each observation to a particular orbit; however, operational processing irregularities make this assignment difficult. In a region where two orbits overlap, the pixels are selected by the order in which the data are entered into the mosaic array; this order is neither reliably recorded in the data nor is it constant in time. Furthermore, the satellite zenith angle limit applied to the data that determines the amount of overlap between orbits is not the same for all orbits nor even the same on both sides of the nadir track in the same orbit. Differences in the processing of VIS and IR data also cause the mosaics to contain data from different orbits for the same location in the polar regions; these data were discarded.

We discovered that the sensitivity of the calculation of TAU to the viewing geometry produced distinctive, spurious features in the geographic distribution of TAU that are not present in the original VIS data distribution when the orbit assignment is incorrect. Using a combination of repeated radiative model analyses and manual inspection of the data in the form of photographic images, we were able to infer the "rules" governing the overlap of the data from different orbits. We estimate that about 5% of the data are still improperly assigned.

Manual inspection of the complete dataset was also performed to remove occasional large areas of spurious data or noisy scan lines. This inspection was performed separately from the inspection required to determine orbit sequences. Difficulties with reading magnetic tapes produced on old tape drives also caused loss of data. For the 4 months of data analyzed, the percent-

ages of the total (possible) data used are 89% (January), 73% (April), 94% (July), and 58% (October).

b. Temperature and humidity data

Atmospheric temperature and relative humidity profiles are needed to calculate the atmospheric effect on the IR radiances and to infer PC and ZC from TC for clouds located at any height in the troposphere. Profiles for each geographic location and date are daily averages of the gridded analyses produced by the National Meteorological Center (NMC) of NOAA. These data represent an analysis (by assimilation in a forecast model) of conventional weather station reports at 0000 and 1200 UTC every day to produce a uniform global map of profiles on standard pressure levels (1000, 850, 700, 500, 300, 200, 100, 50, 10 mb). The map grid defines regions of 2.5° lat and long (see McPherson et al. 1979; Rosen and Salstein 1980; and Kistler and Parrish 1982, for more details). The spatial resolution of these data are sufficient to represent the most significant variations in the atmospheric thermal structure; when calculating IR radiances for the higher resolution SR data, the nearest temperature/humidity profile is used.

Atmospheric temperature structure is dominated by relatively large-scale (>500 km) features, but the data available for NMC upper-air analysis is also very sparse, making it difficult to evaluate the effects of the analysis on the results. Rosen and Salstein (1980) find good agreement (to within about 2–4 K) between their own analysis of the radiosonde data and the NMC results. Comparison of current satellite-retrieved temperature profiles and the gridded analysis based on them suggests little increase in errors over the original data, except for summer continental areas where diurnal variations produce discrepancies as large as 5 K at low levels. Using estimates of the satellite profile uncertainties (Smith et al. 1979; Phillips et al. 1979), and our comparisons of the NMC data with satellite profiles suggests an uncertainty in the NMC profiles of ≈3–4 K. This compares well with a direct estimate of the uncertainties in 1975–79 using aircraft data (Jasperson and Nastrom 1984).

The NMC data report the vertical distribution of water vapor as relative humidity profiles, RH(p). Since atmospheric humidity exhibits more small-scale structure than do temperatures (e.g., Maul 1981), the accuracy of the gridded analysis humidity is lower, especially over oceans. Rosen and Salstein (1980) find errors in the NMC humidities that are at least 20%–30% with a bias towards higher values. Uncertainties in water vapor amounts must, therefore, be taken to be as large as 30%.

c. Surface pressure, temperature, and humidity

To determine the surface pressure (i.e., locate the surface in the temperature profiles), we use the reported geopotential heights of the standard pressure levels, together with a surface topographic height dataset (resolution averaged to 2.5°) to calculate the surface pressure:

$$\mathrm{PS} = P_i \exp\{g(Z_i - \mathrm{ZS})/[0.5R(T_i + \mathrm{TS})]\} \quad (2)$$

where $Z_i = Z_{ig}/0.98$ is the height of the standard pressure surface, P_i, which has a geopotential height of Z_{ig} and temperature, T_i; and PS and TS are the surface pressure and surface air temperature for a surface height, ZS. Here R and g are the atmospheric gas constant per unit mass and the gravitational acceleration. [Equation (2) is the equation used to calculate the geopotential height from the measured temperatures in the NMC documentation.] The pressure surface, P_i, used in (2) is P_1 = 1000 mb when ZS < Z_1 or the closest pressure surface for which ZS < Z_i when ZS > Z_1. This procedure provides only an estimate of the surface pressure because of the unknown effects of the NMC forecast model assimilation process. Comparison of the surface pressures obtained from the NMC data using (2) to seasonal climatologies does not show any significant disagreements.

The PS is calculated using the NMC value of TS (surface air temperature) in (2). The surface temperature value used to calculate IR radiances is obtained from a combination of satellite clear sky radiances and the NMC data as described in section 3. This combination is necessary because the NMC surface temperature analysis does not accurately reflect the surface "skin" temperature measured by the satellite, does not account for the diurnal cycle, has too low spatial resolution, and has some additional problems producing unacceptably large errors, as discussed next.

We attempted our first analysis of the satellite data using the NMC values of TS directly; however, a large number of problems were apparent in the results. Investigation of the causes identified four problems with the NMC surface temperatures. First, comparisons of the NMC surface temperatures with the actual reports of the global surface station and ship network and with the geographic patterns of IR brightness temperatures observed by the satellite in manually selected, cloud-free regions reveal deficiencies of the NMC surface data associated with poor spatial resolution. Over oceans the low density of ship reports, particularly over the Southern Hemisphere oceans and near sea ice, leads to errors caused by attempts to extrapolate other observations into these regions. Land surface temperature difficulties arise because the resolution of the NMC data (≈250 km) fails to resolve sharp changes in surface temperatures, especially at coastlines, and associated with topography. Second, difficulties apparently caused by the NMC Hough analysis technique produce spurious spatial oscillations of surface temperatures associated with sharp temperature discontinuities, for

example, at the coasts of North and South America (Fig. 2). This feature appears to be common in the NMC gridded analysis for surface temperatures, e.g., the features shown in Fig. 2 are found in the monthly mean values. As the figure illustrates, the oscillations have large amplitude and can extend over large distances. Third, since the NMC analysis does not (directly) account for diurnal variations in surface temperature, large differences between the NMC values and station temperatures nearest the satellite overflight time occur. Fourth, the unknown geographical variation of surface emissivities and the changing relationship of surface "skin" and air temperature (see discussion in Minnis and Harrison 1984a; Stowe et al. 1988a; Rossow et al. 1989) make proper determination of the skin temperature from the air temperature very difficult. For all these reasons, we retrieve the surface temperature from the satellite radiances in clear scenes.

Surface relative humidity over the ocean is obtained by extrapolation (when the surface pressure is >1000 mb) of atmospheric values. Over land, extrapolation to the surface is performed to maintain a constant water vapor mixing ratio below the 1000 mb level, which is more consistent with the drier conditions over land.

d. Ozone column abundance

Since ozone occurs primarily in the stratosphere, above all clouds, we can calculate its effect on the VIS radiances as an independent absorption located in a single layer. Total column abundances of ozone are specified by the last year of a zonal, monthly mean climatology obtained by the SBUV instrument on NIMBUS-4, covering the years 1974 through early 1977 (Hilsenrath et al. 1979; Hilsenrath and Schlesinger 1981). This climatology is very similar to that of London et al. (1976).

Uncertainties in the values obtained by the SBUV are estimated to be ≈15%. Some additional error is added to our analysis because of the neglect of the actual synoptic variability of ozone abundance, e.g., as observed by the TOMS instrument on NIMBUS-7 (Bowman and Krueger 1985). Combining these two error sources gives an uncertainty ≈20% in the O3 abundance.

e. Surface reflectance

Although there are several global surface albedo datasets available (e.g., Hummel and Reck 1979; Mat-

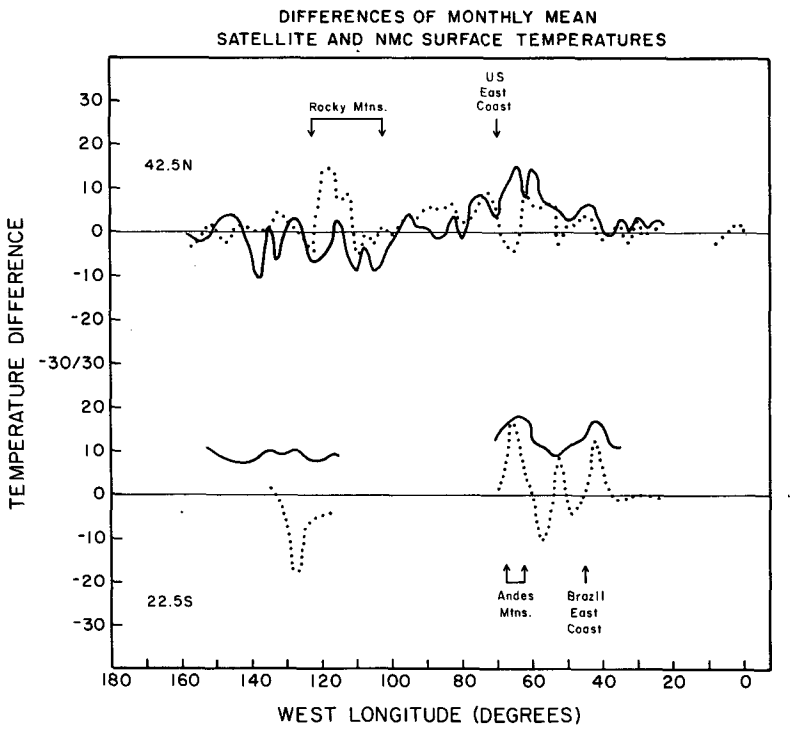

FIG. 2. Differences between monthly mean surface temperatures from the NMC gridded analysis and from the SR analysis as a function of longitude for two latitudes, 42.5°N and 22.5°S, and two months, January and July 1977. The solid curves are for January and the dotted curves are for July.

thews 1985; Posey and Clapp 1964), these provide broadband albedos rather than the narrowband reflectances that we need to calculate VIS clear sky radiances. We attempted to combine the land classification database of Matthews (1983, 1985) with literature values of the visible reflectance; however, we found that the (1° by 1°) spatial resolution was too coarse to resolve important details. Also, the literature values for certain surface types, especially deserts, fail to represent the actual geographic variability of the reflectances (Matthews and Rossow 1987). Consequently, as with surface temperature, we found it necessary to retrieve the surface reflectance by direct analysis of the clear sky radiances obtained from the satellite, as discussed in section 3.

f. Other datasets

Five other datasets are used to describe surface types as a function of location and to assist in the separation of clear and cloudy scenes. Each location on the globe is specified as land or water using a 0.1° resolution world map (derived from Masaki 1972), while topographic heights above mean sea level are taken from the 1° resolution Scripps topography (Gates and Nelson 1975). Vegetation type and soil type are specified by data from Matthews (1983, 1985) and from the Oxford World Atlas (Cohen 1973), respectively. A snow latitude/altitude climatology as a function of month is taken from (Lamb 1972). All of these datasets are used in a statistical analysis of the satellite radiances to remove cloud contamination from the clear sky VIS and IR radiances and to detect the presence of snow and sea ice cover (described in section 3).

3. Method

Satellite observations of a geographic region over a period of time produce a distribution of radiance values due to the space and time variations of the surface, atmosphere, and clouds (Sèze and Rossow 1989). These distributions exhibit characteristic structures representing different contributions from changing surface and meteorological conditions (e.g., Fig. 3). Surface conditions can range from very bright and very warm (Sahara, Fig. 3a) to very dark and warm (tropical Atlantic, Fig. 3d) to dark and cooler (North Atlantic, Fig. 3c). The time and space variations of surface properties can be small (tropical Atlantic exhibits sharp mode at low VIS, high IR in Fig. 3d) or large (Sahara shows broader distributions about the mode in VIS and IR in Fig. 3a). Clouds can be predominantly scarce and thin (cirrus over the Sahara causing low frequency "tail" in the distribution of VIS and IR in Fig. 3a), persistent, low-level and bright (South subtropical Atlantic in Fig. 3e), highly variable in properties (tropical Atlantic in Fig. 3d), or less variable (North Atlantic, Fig. 3c).

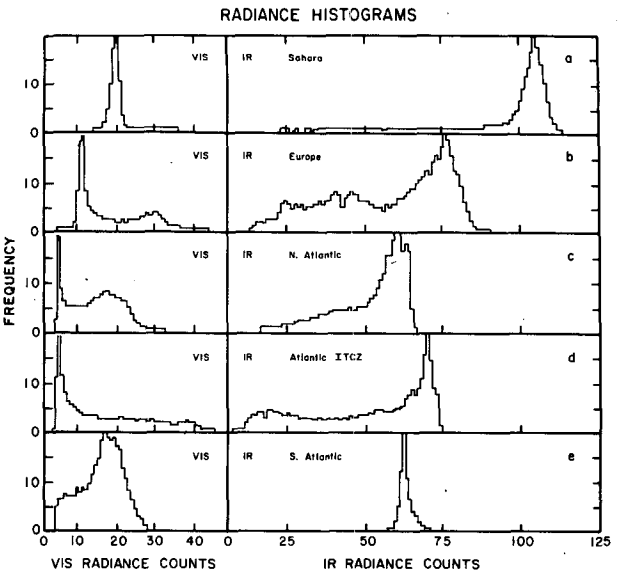

FIG. 3. Sample one-dimensional VIS/IR radiance histograms illustrating the shapes for different situations: (a) Sahara, (b) western Europe in summer, (c) North Atlantic in summer, (d) tropical Atlantic in the intratropical convergence zone, and (e) South subtropical Atlantic in the marine stratus area near Africa. The histograms show the frequency of occurrence of radiances in small (300 km × 300 km) regions accumulated over 15 days. Count values represent VIS and IR radiances measured by METEOSAT-2 ranging from dark to bright and cold to warm, respectively (cf. Sèze and Rossow 1988).

The first objective of cloud analysis methods is to identify and classify appropriate subsets of these distributions (in this case, to separate radiance values representing clear and cloudy scenes). The various cloud detection methods that have been proposed (Table 1 is a survey of cloud algorithms) differ in the method used to identify these subsets (see Rossow et al. 1985). Some methods make use of differences in the magnitude of small-scale spatial radiance variations (Harris and Barrett 1978; Coakley and Bretherton 1982; Coakley and Baldwin 1984), while others use the similarity of radiance values in small regions to identify homogeneous subregions (Desbois et al. 1982; Simmer et al. 1982; Phulpin et al. 1983; Arking and Childs 1985). A more common strategy is to select an extremum of the radiance distribution (e.g., the maximum temperature) to identify clear regions. The extremum may be related either to spatial variation or time variation (Arking 1964; Miller and Feddes 1971; Chahine 1974; Chahine 1977; Reynolds and Vonder Haar 1977; Minnis and Harrison 1984a; Coakley and Baldwin 1984). Similar approaches are also used to isolate cloud-free scenes to study surface properties (e.g., Pinty and Szejwach 1985; Saunders 1985). Gutman et al. (1987) identify clear conditions with the minimum spatial variance in small-image subregions over time, among other tests. Other more complicated strategies that combine several of these ideas are possible (see

Rossow et al. 1983, 1985; Coakley and Baldwin 1984; Minnis et al. 1987; Saunders and Kriebel 1988). An alternative to these satellite-only approaches is to use another dataset to specify clear scene radiance values (e.g., specifying clear sky IR brightness temperature from surface temperature data) and identify as cloudy any satellite-measured values which are different from the values predicted by this other dataset (Koffler et al. 1973; Shenk et al. 1976; Fye 1978; Stowe 1984; Stowe et al. 1988). The method presented here utilizes tests of both spatial and temporal homogeneity, augmented by information from several surface datasets, to identify satellite clear scene radiances.

Our method analyzes the satellite radiance data twice: first, to determine the clear sky radiances and retrieve surface properties and, second, to identify the cloudy sky radiances and retrieve cloud properties from them. Clear sky radiances are obtained from several values near the extremes (minimum reflectance and maximum temperature) in the time distribution of radiances at each location to preserve maximum spatial resolution. A test for small time variability is used to identify average clear conditions. An additional test for small spatial variability of the radiances is used to eliminate any remaining cloud contamination. The clear VIS and IR values are compared to a clear sky radiative transfer model, that includes only the effects of the atmosphere and surface, to obtain surface reflectance, RS, and surface temperature, TS, respectively; these values are taken to represent monthly mean values. The monthly mean land reflectances and ocean temperatures are used with daily NMC temperature/humidity profiles to calculate the clear sky radiances for each day in the month, while daily land surface temperatures are constructed from the satellite-based monthly mean values and the day-to-day deviations of the conventional surface temperatures from their monthly mean values. A model of ocean reflectances is used to predict clear VIS radiances. The accuracy of these assumptions is evaluated in section 4a (see also Ro89).

Once the clear sky radiances (or surface properties) are specified from the first analysis, all the radiances are compared to a cloudy sky radiative transfer model in the second analysis to retrieve cloud optical depth, TAU, from the VIS radiances and cloud top temperature, TC, and height, ZC, from the IR radiances. Differences between the measured radiances and those inferred from the specified surface and atmospheric properties at each location and time are interpreted to be caused by the presence of clouds; VIS and IR radiances that are nearly equal to the specified clear sky values have values of TAU and ZC near zero. "Clouds" are identified by a bispectral threshold: cloudy image pixels are defined to be those with values of TAU and ZC larger than the values that are caused by errors in the specification of surface and atmospheric properties.

All the steps in the analysis procedure are described in more detail in the following parts of this section. Section 4 presents the results of tests conducted to evaluate the success of the method; however, the selection of particular algorithm steps and parameters was an iterative process that incorporated the results of the validation studies back into the algorithm design. Thus, the material in section 4 summarizes the evidence providing validation of the results and supporting the choice of the specific algorithm characteristics described in this section.

a. Radiative transfer models

The optical constants in the radiative models for VIS and IR radiances are adjusted to account for the spectral response of the NOAA-5 SR (Fig. 1) and to simulate the observed spectral radiances as a function of viewing geometry. Since the same procedure and atmospheric data are used to retrieve surface properties from satellite-measured radiances for clear scenes, any difference between a particular satellite radiance and the model predictions with no clouds is interpreted to be due entirely to the presence of cloudiness. Cloud cover and all optical properties are assumed to be homogeneous in a single SR FOV, representing an area 8×8 km at nadir. The cloud parameters retrieved by this analysis are, strictly speaking, model dependent values which make sense only in the context of the particular radiative model. Nevertheless, we will argue that these cloud parameters are not completely divorced from actual cloud properties and estimate, in section 4, the magnitude of errors produced by accepting these values as correct physical quantities (see also, Arking and Childs 1985; Rossow et al. 1985).

1) INFRARED CHANNEL MODEL

The infrared channel of the NOAA-5 SR measures radiances at 10–12 μm (Fig. 1b) which are significantly affected only by emission from the surface, clouds and atmosphere and by absorption by atmospheric water vapor and clouds. Scattering by clouds is a very small effect since the maximum reflectance at these wavelengths is about 2% for liquid water and less for ice (Hale and Querry 1973). Likewise, surface reflection of IR is also small (e.g., Prabhakara and Dalu 1976; see also Minnis and Harrison 1984a) so that total surface emission can be approximated by black-body emission. Thus, all IR scattering is neglected in the model calculations. The model clear atmosphere is constructed from a black-body surface overlaid by absorbing atmospheric layers defined by the NMC pressure levels (1000, 850, 700, 500, 300, 200, 100, 50, and 10 mb, where pressure levels below the local surface are eliminated). Temperature and humidity profiles are obtained from the NMC data for each day and location. Clouds, when present, are represented as

opaque, black-body layers with a temperature equal to the atmospheric temperature at the cloud top pressure. ("Thin" or transparent clouds are treated separately.)

The absorption coefficient of water vapor is calculated from a temperature-pressure dependent formulation of the continuum absorption based on that of Roberts et al. (1976), weighted by the spectral response of the NOAA-5 SR. For modeling simplicity this parameterization neglects the absorption due to weak lines in this part of the spectrum. The emission and absorption are calculated in each atmospheric layer assuming a temperature variation within the layer such that the Planck function varies linearly with height.

The model is used to convert the NMC physical temperature and humidity profiles into *brightness* temperature profiles at two satellite viewing zenith angles (cosine of the viewing zenith angle is $\mu = 0.5$ and 1.0) by calculating the satellite-measured brightness temperatures with a black-body placed successively at the surface and at each standard pressure level. Clear scene radiances are calculated for a range of surface temperatures above and below the original NMC surface temperature value, using monthly mean temperature and humidity profiles. Comparison of the observed clear IR brightness temperatures with these predicted clear scene brightness temperatures is used to infer the black-body surface temperature, TS, corresponding to the observed clear IR radiance. Retrieval of cloud top temperature, TC, and height, ZC, is done by comparison of observed IR brightness temperatures to the brightness temperature profiles obtained from the local daily NMC temperature and humidity profiles, with the surface temperature retrieved from the analysis of the clear scene radiances. The retrieved surface temperatures are joined to the NMC atmospheric profiles with the same surface relative humidity; i.e., if the satellite-based surface temperature is different from the original NMC surface temperature, the absolute humidity is changed to keep relative humidity the same.

When temperature inversions occur, there is more than one value of ZC that is consistent with the observed IR brightness temperature. The ambiguity of this double-valued relation between TC and ZC cannot be resolved with a single observation. In these results, the largest ZC value corresponding to the observed brightness temperature is selected, thereby introducing a possible bias. Examination of the NMC temperature profiles shows that such conditions are rare, since we avoid the polar winter; however, the NMC profiles probably underestimate the occurrence of shallow inversions, especially those occurring near the ocean surface.

2) VISIBLE CHANNEL MODEL

The only significant gaseous absorption within the bandpass of the NOAA-5 SR visible channel (Fig. 1a) is that by ozone (Lacis and Hansen 1974). The primary radiative process at this wavelength is scattering of solar radiation by gas and cloud.[3] The cloudy atmosphere model is constructed with five layers: ozone absorbing layer, Rayleigh scattering layer above the cloud, cloud (Mie) scattering layer, Rayleigh scattering layer below the cloud, and an isotropic reflecting surface, except for water-covered locations which are treated in a separate model. The clear atmosphere model has an ozone layer, no cloud, and a single Rayleigh scattering layer.

Ozone absorption occurs in the Chappuis band, which is about 0.3 μm wide, centered approximately at 0.6 μm. It is calculated using absorption coefficients, taken from Inn and Tanaka (1953), and the parameterization of Lacis and Hansen (1974), which corrects for the change in the spectrum of Rayleigh scattered sunlight with changing scattering geometry. We define an effective ozone absorption coefficient to account for the wavelength variation of the solar spectrum, the spectral dependence of ozone absorption, and the response function of the SR. Ozone column abundances as a function of latitude and month are taken from the NIMBUS-4 SBUV climatology (Hilsenrath et al. 1979).

Atmospheric Rayleigh scattering occurs in two layers, one above the cloud with an optical depth proportional to the cloud top pressure and one between the cloud layer and the surface with an optical depth proportional to the difference between 1013 mb and the cloud top pressure. The proportionality constant is adjusted to account for the wavelength variation of sunlight, ozone absorption, and the spectral response of the SR (Hansen and Travis 1974; Lacis and Hansen 1974): for a clear column, the Rayleigh optical depth is 0.063.

The VIS radiance model without clouds is used to produce a table of VIS radiances as a function of viewing geometry and surface reflectance. All surfaces, including open water, are assumed to be isotropic reflectors for the retrieval of surface reflectances from clear radiances. Comparison of clear scene VIS radiances to the model values provides values of the surface reflectance, RS, for each location.[4] These retrieved surface reflectances are used in the cloudy scene model for all land locations and for water locations determined to

---

[3] Aerosol scattering may contribute a similar or somewhat larger amount of scattering as the gaseous atmosphere. Since this effect is neglected in the analysis of both clear and cloudy scenes, the average aerosol effect is included in the retrieved surface reflectance and the more variable part of the aerosol is included as cloud effect.

[4] A code error resulted in the neglect of ozone absorption in the retrieval of the surface reflectances. This error reduces surface reflectance values by about 1%–2% for dark (<20% reflectance) surfaces at low and middle latitudes and by 5%–15% at high latitudes (see Matthews and Rossow 1987). Ozone absorption was included in the cloud analysis step, which means that the TAU values retrieved for thin clouds are overestimated slightly.

be covered by ice. For open water the retrieved values of RS are replaced by a model of anisotropic reflection from a rough water surface, calculated as Fresnel reflection, in a separate version of the cloudy scene model.

Field measurements indicate some anisotropy of land surface reflectances, but the angular variations, at wavelengths near 0.6–0.7 μm, are generally small (Holben and Fraser 1984; Duggin 1985). Fresh snow exhibits relatively weaker viewing geometry dependence than vegetated surfaces, except for a specular component that becomes more prominent for aging snow (Warren 1982). The reflectance of snow-covered land surfaces is a complicated combination of snow and vegetation reflectances; hence, the retrieval of specific reflectance values for each location every month is expected to represent the actual value more accurately than it can be specified from other measurements. The largest difficulty with snow-covered land arises from uneven topography and different masking depths for different vegetation types, as discussed in section 4 and in Ro89. Moreover, variations of snow cover are geographically uneven and occur on time scales less than 1 month. The sun-synchronous orbit geometry of NOAA-5 produces only a limited variation of viewing geometry and generally avoids specular reflection geometry (cf., Robock and Kaiser 1985); thus, retrieval of a new reflectance each month, averaged over several values with different viewing geometries, minimizes the angle dependence. The accuracy of these reflectances is discussed in more detail in Ro89.

Ocean surface reflectance is anisotropic and variable because of wind roughening of the surface. Although ocean reflectance values are also retrieved from clear scene VIS radiances, they are primarily used to aid in proper identification of clear scenes and to remove cloud contamination. However, whenever sea ice is detected in the clear radiance analysis step, the retrieved reflectance is used. For open ocean (and large lakes), the reflectance is modeled as Fresnel reflection from a water surface with a statistical population of wave slopes taken from Cox and Munk (1956). This formulation gives a solar zenith angle dependence on wind speed (Hansen et al. 1983):

$$\mathrm{RS} = 0.021 + 0.0421x^2 + 0.128x^3 - 0.04x^4 + [3.12/(5.68 + \mathrm{WS}) + (0.074x)/(1 + 3\mathrm{WS})]x^5 \quad (3)$$

where $x = 1 - \mu_0$, μ_0 is the cosine of the solar zenith angle, and WS is the surface wind speed. (A similar formulation was developed by Takashima and Takayama 1981.) We use (3) with WS = 5 m s^{-1}, which makes the bracketed part of (3) = [0.29 + 0.0046x], which agrees to within 0.1% for $\mu_0 \geq 0.5$ with the results of Takashima and Takayama (1981) and agrees to within 1% with the data shown by Kondratayev (1969, 1973) for $\mu_0 \geq 0.4$. We extended this formulation to include satellite zenith and relative azimuth angle dependence.

For the cloudy scene model a single cloud layer is included; conservative Mie scattering is calculated for a homogeneous, plane-parallel layer composed of water spheres with an effective radius of 10 μm and an effective size variance[5] of 0.15 μm (Hansen and Travis 1974). The model predicts the VIS radiances as a function of total cloud optical depth, viewing geometry (μ_0, μ, and the relative azimuth, ϕ[6]), surface reflectance, and cloud top pressure.

The radiance observed by the NOAA-5 SR is simulated by combining the four scattering layers using the invariant imbedding procedure (Sato et al. 1977), which is a variation of the doubling/adding method that allows for the efficient combination of homogeneous layers with arbitrarily large optical depths. The model predictions are calculated once for all combinations of a range of values of TAU (0 to 100), viewing geometry angles (0.1–1 for μ_0, 0.5–1 for μ, and 0°–180° for ϕ), surface reflectance (0%–100%), and cloud top pressure (100–1000 mb). These results are used in tabular form to retrieve a value of TAU from a visible channel radiance, where all the other quantities are specified from other datasets or earlier analysis steps as described above. The cloud top pressure is inferred from the IR radiance. The table intervals and the interpolation sequence are designed to optimize accuracy against table size. The order of interpolation is geometry, surface reflectance and cloud top pressure. Each entry in the table represents a polynomial fit with up to five coefficients relating the radiance and TAU for each combination of μ, μ_0, ϕ, RS and PC:

$$\ln(\mathrm{TAU}) = c_1 + c_2x + c_3x^2 + c_4x^3 + c_5x^4, \quad (4)$$

where x = VIS radiance (normalized by total solar intensity). The number of coefficients is variable; it is selected to insure a "fitting" accuracy of better than 10%. Errors due to interpolations were tested and found to be <10% (see section 4).

When surface reflectances are >50%, the difference in the angular dependence of radiation reflected from clouds and (assumed) isotropic surfaces can make cloudy scenes darker than clear scenes in the model for low values of TAU and some viewing geometries; i.e., the relation between TAU and VIS radiance becomes double-valued: below the value of VIS corresponding to clear conditions there are two values of TAU which produce the same radiance. There is also a value of TAU, in addition to zero, consistent with

[5] Effective radius and variance are cross-section weighted values obtained assuming a "gamma" distribution of droplet sizes (Hansen and Travis 1974).

[6] Relative azimuth represents the scattering azimuth which is 180° different from position azimuth, i.e., specular reflection occurs at $\mu = \mu_0$ and $\phi = 0°$.

the clear sky value of VIS. This nonuniqueness cannot be resolved for a single observation. In this study we use only the portion of the VIS/TAU relation that is monotonically increasing, which introduces a bias in TAU values, since cloudy scenes are brighter than clear scenes only for TAU $\geq$ 10 for surface reflectance $>$ 50%. (See discussion in Part II concerning the mean TAU values for the polar regions.)

b. Surface property retrieval

The first step in the cloud retrieval analysis obtains and defines measures of the satellite radiance values that represent clear sky conditions at each location. We use the radiative transfer models to convert the clear VIS and IR radiances into surface reflectances and temperatures, respectively. The simplest and most common method to obtain surface reflectance and temperature is to assume that clear sky is indicated by the lowest reflectance and highest temperature observed in a region (Arking 1964; Desbois et al. 1982; Simmer et al. 1982; Arking and Childs 1985; implicitly in Coakley and Bretherton 1982; see also Coakley and Baldwin 1984) or by times with the lowest reflectance and highest temperature (Reynolds and Vonder Haar 1977). This approach produces a biased measure of the surface properties, because a repeated observation of a single location (or over some spatial domain) leads to a distribution of radiance values (see Fig. 3) with extreme values that can differ significantly from the mean value. Also, selecting a single extreme value makes the final outcome sensitive to the sample size and to rare events that produce unexpected radiance variations (e.g., cloud shadows; cf. Sèze and Desbois 1987). The magnitude of this bias was estimated by accumulating SR radiance measurements over the ocean (representing a homogeneous surface) for a 30-day time period; the resulting minimum reflectances (maximum temperatures) were 4% below (3 K above) the mode values, representing a bias of about one to two times the standard deviations of the distributions. Atmospheric and viewing geometry variations, actual surface variations, and radiometer noise all introduce variations; use of the absolute extremum selects for a rare condition when all these factors combine in a particular fashion. Although threshold methods that use this approach specifically use larger thresholds to compensate for the bias, this reduces the sensitivity of these methods to thinner or low-lying clouds which cause only small changes in the measured radiances. The sample size dependence of the bias makes the results dependent on the nature of the surface and the amount of cloudiness present.

The method we have tested to improve retrieved surface properties retains the simplicity of the extremum approach, but attempts to recover the average of the actual distribution of values caused by atmospheric variations, radiometer noise, and actual surface variations.[7] (Stamm and Vonder Haar 1970, and Minnis and Harrison 1984a, propose other solutions to this problem.) The resulting surface reflectance and temperature are taken to represent the monthly mean values at each location; section 4 presents tests of this hypothesis.

The first part of the clear sky retrieval is to extract from the month-long visible (VIS) and infrared (IR) radiance records at each location the VIS values corresponding to the four largest IR values, called VIS(IRMAX), and the IR values corresponding to the four lowest VIS values, called IR(VISMIN). These values are converted to surface reflectances (RS) and temperatures (TS) using the clear scene radiative models described above to remove the dependence on viewing geometry. Use of extreme values in one channel to select four values in the other channel recovers the actual clear sky distribution of radiances because radiometer noise and the effects of daily variations of the atmosphere are essentially uncorrelated in the two channels. Examination of the variations of the radiances in the two channels also shows them to be more strongly correlated for cloudy scenes than for clear scenes. (See results presented by Desbois et al. 1982, Desbois and Sèze 1984, for example; see also Sèze and Rossow 1989.) Hence, the extreme values are more likely to represent clear scenes, but the associated values in the other channel will not be biased as they are by using their extreme values directly (see also Bernstein 1982).

Next, we test the standard deviation of the four values of RS and TS: if $\sigma(\mathrm{RS}) \leq 5\%$ and $\sigma(\mathrm{TS}) \leq 3$ K, then the average of all four values is taken to represent the surface property. This test explicitly assumes that the time variations of radiances, due to causes other than the occurrence of clouds, are smaller than those produced by the presence of clouds. If the standard deviation is too large, then cloud contamination is assumed to be present and the RS value corresponding to the lowest IR value and the TS value corresponding to the largest VIS value are discarded. If the standard deviation is still not acceptable, no value of RS or TS is reported. Comparison of these results to analyses using five–ten values, rather than four or three, and to the complete radiance distributions shows that the method generally recovers the mode VIS and IR values, within 2% and 2 K, respectively.

These particular limits on the variances were selected by examination of radiance histograms representing all the observations over January and July for many

[7] Clear radiances in this dataset also vary because the location of the SR FOV, which is smaller than the mosaic grid area, is variable within the grid area. Consequently, the average surface properties also represent an average over the grid area.

different climate regimes over the globe. These histograms show a characteristic shape (similar to those shown in Fig. 3): a narrow peak near one extreme (low VIS and high IR), implying a small variance near the peak value, and a broad distribution of values ranging up to the other extreme (high VIS and low IR). The highly asymmetric distribution seems associated with the observation that clear scenes are generally darker and warmer than cloudy scenes with substantially less variability (Sèze and Rossow 1989). The typical magnitude of the histogram variances near the mode value, representing the clear scene values, is used in the test discussed above. In Fig. 3e the histogram for a highly cloudy location shows why this approach may not always succeed: this relatively narrow IR distribution represents almost total coverage of the scene by marine stratus clouds at all times.

The third part of the procedure examines the spatial variations of the radiances to eliminate remaining cloud contamination, which is produced by clouds that cause only small variations in the radiances or by clouds that are both persistent and relatively constant in optical properties (small time variations, e.g., the clouds in Fig. 3e). The first form of contamination occurs because of the differing sensitivities of the VIS and IR channels: the VIS channel is insensitive to cirrus but cirrus has a strong effect on the IR channel, while the IR channel is insensitive to low, broken clouds which can have large effects on the VIS channel. The strategy in the third step is to intercompare the RS values for similar surface types from different parts of the globe to detect any anomalous values. The assumption is that variations with location of the surface conditions of similar surface types are smaller than the variations produced by clouds.

This process requires classification of the surface into homogeneous types. Each latitude zone (90°–60°S, 60°–30°S, etc.) is divided into land and ocean. Land is further subdivided into different soil types [Oxford World Atlas (Cohen 1973)] and vegetation types (Matthews 1983, 1985) for reflectances and different topographic altitude ranges for temperatures. In addition, a separate land type is associated with snow cover.

A land location is labeled snow-covered if its latitude and altitude allow for snow cover during the particular month, based on climatology (Lamb 1972), and the mean clear sky radiance values are RS > 35% and TS* < 273 K. In this case, TS* is the average of the largest IR values used to obtain RS, rather than the reported value of TS. An ocean location is labeled as sea ice covered if mean RS > 20% and TS* < 271 K. The success of this procedure is summarized in section 4 and discussed in more detail in Ro89.

For each latitude zone the RS values for pixels with the same surface type are collected into a histogram. If the width of the histogram is sufficiently small (reflectances at frequencies half of the peak frequency are within −4% and +7%), then that surface type is considered homogeneous and RS values which are outside the range on the high side are discarded if they are not labeled as snow or sea ice cover. If no sufficiently small-width histogram is available for a location then no test is performed; this occurs primarily in arid regions at low latitudes and over permanent sea ice cover. These histograms are discussed in more detail for land in Ro89 and in Matthews and Rossow (1987).

Similar histograms of TS values for similar latitudes and topographic altitudes were constructed. No useful test for cloud contamination was found since most of the remaining cloud contamination is apparently low-level, broken cloudiness which does not cause a significant change in the IR radiances (see section 4). Thus, only the tests on the reflectances are retained to remove cloud contamination. The variation of land surface temperatures over 30 days is large enough, however, that further refinement of the TS values is needed as discussed below.

The final part of the retrieval of surface properties from the satellite data is the filling of "holes" in the global maps of RS and TS. There are two types of holes produced by the tests described in steps 1–3: scattered, isolated pixels for which no result is obtained; and small (~200 × 200 km), persistently cloudy regions with no results. The former type occurs most frequently in regions of large, but variable, cloud amount (e.g., the ITCZ and midlatitude storm tracks), suggesting that it is the result of the low frequency of occurrence of clear sky (cf., Fig. 3e). In other words, these are locations where the clear radiances do not occur frequently enough to form a peak in the total distribution. These holes are filled by the average RS and TS values over a 5 × 5 array (≈100 × 100 km) centered on the hole, if more than 50% of the values are present. The small regions, on the other hand, are caused by even more persistent cloudiness (western Pacific ITCZ and monsoon regions) or by rapidly changing surface conditions (active sea ice boundaries in the Davis Strait or Weddell Sea or in regions near the snow-melt line). When the surface properties are as variable as the cloudy atmosphere, then the clear-sky peak in the radiance distribution is blended with the cloudy sky distribution. RS and TS values in these regions are filled by the average value over a larger area (21 × 21 array, ~500 × 500 km). Examination of the radiance histograms accumulated for a month over regions varying in size from (100 km × 100 km) to (1000 km × 1000 km) shows that the spatial variations of clear sky radiances are, generally though not always, small (see also Desbois et al. 1982; Coakley and Bretherton 1982; Minnis and Harrison 1984a; Desbois and Sèze 1984; Sèze and Rossow 1989), so that the 5 × 5 filling probably produces a good estimate of the actual clear sky radiances at a particular location, while the 21 × 21 filling produces a less accurate estimate. (In mixed land-

water regions, holes in each type are filled only by values from the same type.)

To improve the land values of TS used for cloud detection, the daily deviation of the NMC surface temperature values from their monthly mean is calculated for each location. This deviation is added to the TS value retrieved from the satellite data. The underlying assumption is that the complete temperature record is formed, approximately, by the linear sum of the diurnal variation and the synoptic variation. By replacing the NMC monthly mean by the satellite monthly mean value, we correct for the time-of-day bias between the NMC and satellite observations and the difference between surface observable (air temperature) and satellite observable (skin brightness temperature) at that time of day. By adding the synoptic deviations of the NMC temperatures to the satellite monthly mean value, we attempt to reproduce the correct day-to-day variations of the clear sky radiances. The validity of these assumptions is tested in section 4 and discussed in more detail in Ro89.

c. *Cloud property retrieval*

The second step in the cloud retrieval analysis compares all observations to the radiative model predictions *including the effects of clouds.* Most clouds are effectively opaque to IR radiation; hence, when TAU is large enough (see below), IR radiances are modeled as isotropic emission from a blackbody at the temperature of the cloud top, attenuated by any overlying water vapor. In the first part of the cloud analysis, the observed IR brightness temperatures are compared to the brightness temperature profiles inferred from the local, daily NMC temperature and humidity. The clear scene brightness temperature is placed on these profiles at the proper surface pressure.[8] These profiles are interpolated to the value of μ appropriate to the particular observation using

$$T(\mu) = T(1.0) + 2(1/\mu - \mu)[T(0.5) - T(1.0)]/3. \quad (5)$$

If the observed brightness temperature is between the largest and smallest values on the profile, then TC is set to the physical temperature corresponding to the observed brightness temperature and ZC is the associated altitude above mean sea level of that temperature value. If the observed brightness temperature is equal to or greater than the surface (clear) brightness temperature, no cloud is present, TC = TS, and ZC = 0. (Thus, any low clouds with TC > TS will not be detected.) If the observed brightness temperature is less than any value on the profile, TC is set to the observed value and the value of ZC is set to the height of the tropopause. This initial estimate of cloud top temperature and corresponding height is valid for opaque clouds.

Next, the results of the VIS model calculations are used in tabular form to retrieve a value of TAU from the visible channel radiance for the particular viewing geometry, where the ozone abundance is specified from the ozone climatology, the surface reflectance is specified from the earlier clear scene analysis, and the cloud top pressure is inferred from the IR radiance assuming that the cloud is opaque. The observed value of VIS is compared with the table values. If the observed VIS radiance is equal to or less than the lowest model VIS radiance for the specified geometric, atmospheric, and surface conditions, then TAU = 0. If the observed radiance is greater than any value in the table created by the model, TAU is set to its maximum value of 100. Intermediate values of the VIS radiance lead to intermediate values of TAU.

When TAU is small, the interdependence of TAU and TC is treated by an iterative procedure. The initial value of TC is obtained from the IR radiance, assuming the clouds to be optically thick; the related value of PC is then used to retrieve the value of TAU from the visible radiance. If $\mathrm{TAU}/\mu \geq 4$, no correction to these values is made. If $\mathrm{TAU}/\mu < 4$, the effects of reduced emission from the cloud only partly compensates for the increased radiation caused by transmission of radiation from the surface. For these optically thin clouds, the cloud top temperature is recalculated using

$$B(\mathrm{TC}) = [B(T\mathrm{obs}) - B(\mathrm{TS})\exp(-x/\mu)]/[1 - \exp(-x/\mu)], \quad (6)$$

where $x = \mathrm{TAU}/1.24$, $B(T)$ is the Planck function adjusted for the NOAA-5 SR spectral response, and all of the temperatures are brightness temperatures to take account of the water vapor absorption that occurs primarily below the cloud. The new value of TC is associated with a new PC using the NMC profiles. The calculation of TAU is then repeated with the new PC. The whole cycle is repeated until the solution converges (to within 5%); failure to converge causes the whole observation to be rejected about 10% of the time that $\mathrm{TAU}/\mu < 4$, or for about 2% of the total observations.

In Eq. (6) the cloud optical thickness for extinction of infrared radiation is set equal to (1/1.24) times the optical thickness for extinction of visible radiation, which is retrieved from the visible channel analysis. This ratio (calculated between the extinctions at 12 and 0.55 μm), approximates the ratio for the NOAA-5 SR band-center wavelengths of 11.5 and 0.63 μm. The equivalent ratio is (1/0.87) for ice spheres with an effective radius of 25 and an effective size dispersion

[8] Actually, since the clear scene observation is obtained with varying values of μ, the model is used to retrieve surface temperatures which replace the NMC values in the calculation of the two brightness temperature profiles.

of 0.10 μm (representative of the larger particles in ice clouds, see Hansen and Travis 1974); however, theoretical calculations and observational studies suggest that the elongated shapes of ice crystals decrease this ratio by about 20% (Platt 1979; Platt et al. 1980; Platt and Dilley 1981). Given these uncertainties, we adopt the same ratio for all clouds (see section 4).

d. Bispectral threshold

Comparison of the VIS and IR radiances to the radiative model calculations, which include surface properties inferred from the clear scene radiance measurements, detects the presence of clouds by determining whether the particular radiances differ from the predicted clear values. If the clear value of VIS is equal to or greater than the observed value, TAU = 0; if the clear value of IR is equal to or less than the observed value, ZC = 0. Since there are errors in the predicted clear scene radiances produced by radiometer noise, neglected atmospheric variations, residual cloud contamination, and inaccurate treatment of surface radiative properties and variations, there is uncertainty in the comparison of the "clear" and observed radiance values. Detection of clouds cannot be claimed unless the radiances differ from their clear values by more than the estimated uncertainty in the clear sky radiances. That is, the detection "signal," which is the difference between the clear and observed radiance, must be larger than the detection "noise" (see also, Shenk and Salomonson 1972b; Minnis and Harrison 1984a; Rossow et al. 1985). The tests of the method discussed in section 4 were used, not only to evaluate the procedures described here, but also to estimate this uncertainty in the clear sky radiances. These test results led to the conclusion that clouds can be reliably determined to be present in a particular image pixel only if TAU > 1.2 and ZC > 1.4 km. This is equivalent to an uncertainty in the VIS and IR clear sky radiances of 10% and 9 K, respectively.

4. Tests of the method

Validation of cloud algorithm results usually takes the form of verifying the derived cloud cover amount. While we present such comparisons at the end of this section, this approach, by itself, is inadequate and does not always prove definitive. Another possible approach is to separate the validation of cloud detection from the validation of the retrieved cloud properties, including cloud amount; i.e., we can verify that the radiance values have been properly divided into those representing clear and cloudy locations without necessarily verifying a derived cloud amount. This is possible with our method since detection accuracy depends on the accuracy of specifying the clear sky radiances (cf., Rossow et al. 1985); correct clear scene radiances insure that the cloud algorithm will correctly indicate the presence of cloud at a particular location and time, regardless of the values of cloud amount or other properties ascribed to the clouds. Since the clear scene radiances at 0.6 and 11 μm depend primarily on surface properties, about which we have much more information than clouds, we can use a comparison of other conventional surface data with the clear sky or surface properties inferred from satellite data to estimate their error. The results of this validation of the surface properties are summarized in section 4a and discussed in more detail in Ro89 and in Matthews and Rossow (1987). Sensitivity tests of the variation of cloud amount with threshold are combined with the surface property error estimates in section 4b to provide an estimate of the cloud detection error. Note that the estimated error in the retrieved surface properties and the results of the sensitivity studies were used to select the magnitude of the thresholds in the detection step; thus, the discussion in this section provides the supporting evidence for the specific algorithm steps described in section 3.

Once we have determined that clouds are present in a scene, we can then test whether our radiative models provide an adequate description of their effects on the satellite-measured radiances. The adequacy of the retrieved cloud model parameters can be judged both by whether they provide the correct radiances and by whether they provide the correct physical characteristics of the cloud. Obtaining an understanding of the role of clouds in the earth's radiation balance may only require validation in the first sense (see discussion Part II). Although complete validation of the radiation model is beyond the scope of the information in this particular dataset, we present the results of sensitivity studies of the radiative model in section 4c that illustrate the dependence of the retrieved cloud properties on model assumptions and provide an estimate of the uncertainty in the radiances obtained from them. Validation of the cloud properties as actual physical quantities, rather than model parameters (see Part II), involves consideration of the most important determinant of the radiative properties retrieved, the amount of cloud ascribed to each pixel. In section 4d the cloud amount obtained from this analysis is compared with other results to provide one estimate of the cloud cover uncertainty.

a. Validation of surface properties

Uncertainties in the clear scene radiances arise in three ways: undetected cloud contamination of the radiance values identified as clear by the algorithm, inaccuracies in the radiative model analysis that introduce spurious variations in the reconstructed clear scene radiances, and improper treatment of actual

variations of surface properties. The latter two problems arise because the satellite-based measurements of the surface must be inferred from observations under different conditions than exist in the particular cloudy scene. Validation of the clear scene radiance values obtained in this analysis by comparison to other measurements of similar or related quantities is also dependent on the accuracy of the modeled atmospheric and surface radiative effects, but we need focus only on those effects which affect the correct reconstruction of the radiances. That is, some radiative model assumptions do not affect cloud detection because the same assumptions are used in both the clear and cloudy scene models, even though these same assumptions do affect the comparison of the retrieved value to other measurements of the same surface parameter. The key radiative model issues that affect cloud detection are summarized in the discussion of the comparisons as part of the error analysis; in Ro89 we discuss further issues that affect retrieval of accurate surface properties from this type of data.

The studies conducted to validate the clear scene radiances are summarized in Tables 2 and 3. Since the emphasis of this paper is to estimate the error in the cloud properties, only a brief summary of the validation of the surface results is presented. More detailed evidence and discussions supporting the error estimates are provided in Ro89 and in Matthews and Rossow (1987). The key illustration of the accuracy of the derived clear radiances presented here is the good correspondence of the patterns in the space/time distributions of the satellite-based and conventional measures of the surface properties. This correspondence suggests that the relative variations of the clear scene radiances with location and time have been correctly determined. Some particular problems are illustrated by case study results.

TABLE 2. Summary of surface reflectance validation studies.

Type of study	Study description
Statistical	Distribution and variation of retrieval quality flags and their correlation with surface reflectances.
Statistical	Shapes of reflectance distributions for different classes of surfaces and their variation in time.
Statistical	Geographic patterns of monthly variations of surface reflectances.
Statistical	Case study comparisons of daily to monthly distributions.
Data comparison	Average surface reflectances of various surface types compared to literature values.
Data comparison	Correlation of spatial variations to documented changes in vegetation type.
Data comparison	Location of snow and sea ice boundaries compared to other observations.

TABLE 3. Summary of surface temperature validation studies.

Type of study	Study description
Statistical	Distribution and variation of retrieval quality flags and their correlation with surface temperatures.
Statistical	Geographic patterns of monthly variations of surface temperatures.
Statistical	Case study comparisons of daily to monthly distributions.
Data comparison	Distribution of differences between satellite and conventional surface observations.
Data comparison	Monthly mean distributions and variations of surface temperatures compared to other climatologies.
Data comparison	Synoptic variations of surface temperatures compared with conventional surface observations.

1) OCEAN SURFACE REFLECTANCE

The ocean reflectance as a function of viewing geometry is accounted for in the analysis by the model described in section 3b; however, the statistical retrieval of the surface reflectance is used to check the validity of this model by sorting the results as a function of geometry. [Minnis and Harrison (1984a) also use a statistical retrieval to develop an empirical model of planetary reflectance over ocean.] This comparison shows that the model is correct to within $\approx 2\%$ for geometries away from glint conditions ($\mu \approx \mu_0$, $\phi < 10°$); but, as glint conditions are approached, the model reflectance does not increase as rapidly as observed. A similar conclusion is reached from a comparison of the model reflectance to other data (e.g., Kondratyev 1969, 1973; Payne 1972). For the geometries encountered by NOAA-5, the discrepancy reached $\approx 5\%$ near the edge of an individual orbit swath (low μ). Some cloud contamination is also apparent in the retrieved reflectances over the tropical oceans; however, since the ocean reflectance model is used in the final cloud analysis, this has no effect on the VIS radiance analysis.

When sea ice is determined to be present, the ocean model surface reflectance is replaced by the retrieved value of RS. Validation studies focused on both the inferred location of sea ice and the reflectance values measured for sea ice (see Ro89). Comparison of regions identified as covered by sea ice in our results with several climatologies for the Arctic (Wadhams 1981; NOAA 1984; Parkinson et al. 1987) and Antarctic (Alexander and Mobley 1976; Streten and Pike 1980; Zwally et al. 1983) shows good correspondence (within <200 km) in regions with less variability and in seasons with less ice edge activity. In regions where the ice boundary is actively moving, our results show poorer agreement (errors of 300–500 km). Especially in winter, rapid variations in surface conditions caused by

the moving ice combine with low illumination, low temperatures, and high cloud amounts associated with storms to eliminate most surface retrievals. Consequently, the surface properties are "filled in" by the final part of the surface property retrieval procedure, producing reflectance values intermediate between ice and open water. Since the reflectance of open water becomes >20% for $\mu_0 < 0.2$ (Payne 1972), judging the location of the sea ice edge using surface visible reflectance is less reliable under winter illumination conditions. Thus, a comparison of the apparent ice line, judged by the reflectances in these results, to other data suggests an equatorward bias of about 300–500 km, but the surface reflectance values near this edge are also consistent with open water values. The retrieved ocean temperatures (see section 3 and Ro89), when used to judge the sea ice edge, agree better with other data in winter.

There are few climatological data for the reflectances of sea ice that can be used to validate our values. The range of values we obtain, 20%–60%, is consistent with available reports of broadband albedos for the Arctic (Grenfell and Maykut 1977; Barry et al. 1984) and the Antarctic (Kuhn and Siogas 1978). We also obtain generally higher values in the Antarctic than in the Arctic, consistent with these reports. Comparison of our results to the regional Arctic albedos in summer of the same year, obtained from a different satellite by Scharfen et al. (1987), shows good agreement when our results are corrected for ozone absorption.

In summary, the model used for ocean surface reflectance is accurate to within 2% except near glint geometry, where the model is 5% below the observed reflectivity. The uncertainties in the reflectances for sea ice–covered regions are harder to estimate; however, difficulties with the proper identification of clear scenes in these regions and the amount of variation that can occur in a month suggest that the uncertainties could be 10% or more, with the larger errors occurring near the ice margins. Overall, the errors in the modeled ocean surface reflectance are smaller than the effective VIS threshold used, except possibly near the sea ice margins.

2) LAND SURFACE REFLECTANCE

Direct comparison of our surface reflectance values to other sources of measurement is made difficult by the paucity of such information for the narrow spectral interval of the SR (see Matthews 1985; Matthews and Rossow 1987); however, statistical patterns in the geographic distribution of the surface reflectances can be used to estimate the uncertainties in the values obtained in this analysis. A particularly useful approach is to sort the observations of different geographic locations into groups based on classifications of surface type. The hypothesis is that the reflectances of similar surfaces should be approximately the same; hence, the shapes of the resulting frequency histograms of surface reflectances can provide a measure of uncertainties, detect anomalous values, suggest other statistical tests or case studies, or even indicate that the original classification does not form a homogeneous class. Other tests of the retrieved surface reflectances are described in Table 2.

Land surface reflectances obtained from SR were sorted according to soil and vegetation types. Figure 4

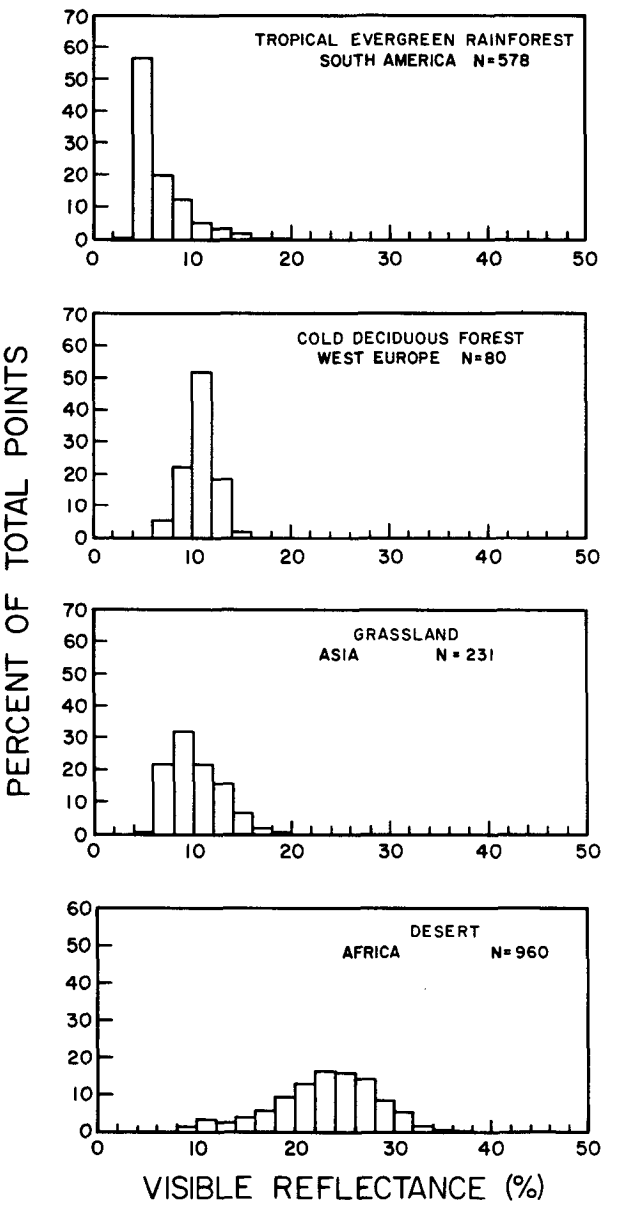

FIG. 4. Distribution of surface visible reflectance values deduced from NOAA-5 SR for four vegetation types: (a) tropical rainforest in South America in January, (b) deciduous forest in western Europe in July, (c) grassland in Asia in July, and (d) desert in Africa in July. The number of 1° square regions included in each category is shown as the value of N (cf. Matthews and Rossow 1987).

illustrates reflectance histograms obtained for four vegetation types from this study. Comparisons of our reflectance values with other observations and the geographic patterns of vegetation and soil distributions are examined more thoroughly by Matthews and Rossow (1987); here we only summarize and illustrate the results. Soil types did not provide any useful discrimination of reflectances, even for desert regions with little vegetation, because soil types are not a good indicator of soil color (Matthews and Rossow 1987). Most of the vegetation types exhibited narrow distributions of reflectance, like those shown in the first two panels of Fig. 4. Average reflectance values from these histograms for all vegetation types agree with available information and the geographic variations of reflectances are consistent with known variations of vegetation type (see Matthews and Rossow 1987).

The histogram for tropical rainforest in Fig. 4 illustrates the effect of cloud contamination on the shape of these histograms: the small population of values extending to 20% reflectance is seasonally variable, being absent in the dry season (July), and varies with location in concert with anomalously low surface temperatures, as inferred from the SR data. Similar comparisons for other vegetation types indicate that cloud contamination occurs over less than 10% of the surface area, primarily in the tropics (Matthews and Rossow 1987).

Since the 0.6 μm channel of SR is relatively insensitive to differences between vegetation types, the narrowness of these histograms places a limit on the errors associated with the removal of atmospheric effects and neglected viewing geometry variations. The estimated error is $\approx$2%–5% and is consistent with field measurements of various surfaces at 0.6 μm, which indicate that reflectance variations with viewing geometry are about 2%–4% for vegetation and 5%–15% for soil surfaces (Kimes 1983; Holben and Fraser 1984; Duggin 1985).

The grassland and desert histograms in Fig. 4 illustrate the large spatial variations of reflectances that can occur for more heterogeneous surface types. It is this large variation that prevents the direct use of surface type information to specify the surface reflectances or the use of spatial averages in the retrieval of surface reflectances from satellite observations for some heterogeneous regions. The specific spatial distributions of reflectances in these heterogeneous regions are confirmed by case studies that compare the derived monthly mean spatial patterns with daily observations; these patterns are accurately described in the SR results (see Ro89).

The constancy of the surface reflectances over the whole year is illustrated by histograms of the differences between the January and July values at each point over each hemisphere; Fig. 5 shows these differences as winter minus summer for each hemisphere. The difference distributions peak at zero with a width of about 3%. Most of the values near the peak are from the oceans; the land areas show a slightly broader difference distribution with a width of 3%–5%. A similar result holds for all other pairs of months. This result shows that the clear sky radiances over the whole globe are nearly constant from one month to the next, verifying the use of a single value for each month.

The exceptions that account for the larger differences in Fig. 5 are regions of snow cover variation. Large variations of surface reflectance caused by changes in snow cover blend the clear radiance distribution with the cloudy radiance distribution, making determination of the surface reflectance more difficult. Currently available information on snow cover reflectances is inadequate to describe the interaction of snow with complicated surface structures, especially vegetation. Reflectance models of snow-covered surfaces also show disagreements with field measurements and each other (Warren 1982).

Our results for snow-covered land are verified in two respects: by proper identification of the presence of

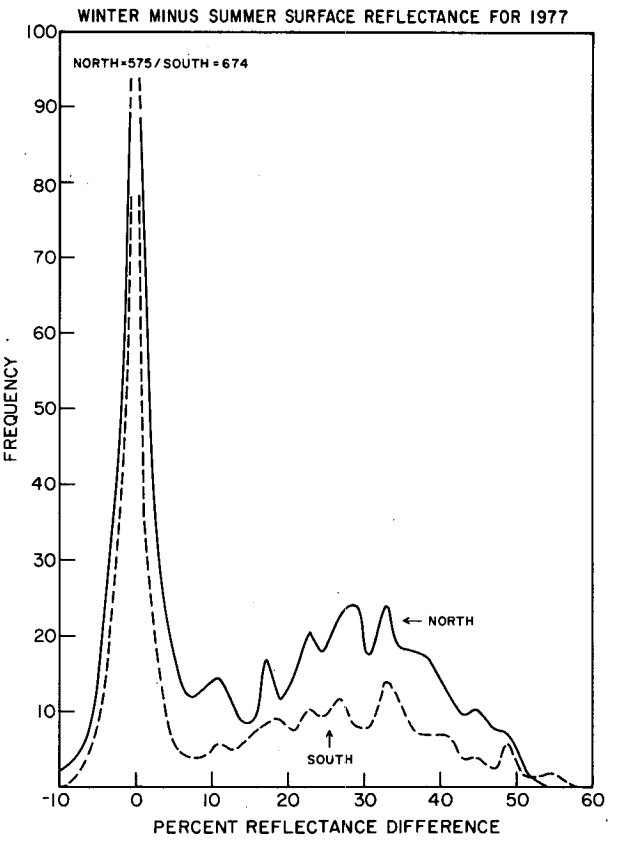

FIG. 5. Hemispheric histograms of surface reflectance difference between January and July 1977 for the Northern and Southern hemispheres. The large peak at zero difference is due to the ocean; the distribution of land reflectance differences also peaks at zero but is somewhat broader than the ocean distribution.

snow and by qualitative agreement with other observations for snow reflectances. Comparison of the snow line location produced weekly by NOAA (1977b) with that obtained from our monthly reflectance values shows good correspondence (within <100 km) in regions where the weekly positions are nearly the same, but poorer agreement (errors of 100–300 km) where the weekly data indicate rapid variations (see Ro89). The amount of space and time variability of snow-covered surface reflectances suggested by these results is consistent with that discussed by Robock and Kaiser (1985). General agreement for the reflectance magnitudes over Antarctica (Carroll and Fitch 1981; Yamanouchi 1983) is also obtained.

In summary [see Ro89 and Matthews and Rossow (1987)], the uncertainty of the reflectances over the majority of the land surface, due to incomplete treatment of atmospheric and angular effects, is judged to be $\leq 3\%$. If the variability exhibited in the various tests and in the January/July differences shown in Fig. 5 is assumed to be entirely due to analysis problems, then the estimated error would be no larger than about 5% [see also, Matthews and Rossow (1987)]. These errors appear to be random. Cloud contamination seems largely absent, except for some areas in the tropics in the wet seasons: the Amazon Basin near the coast of Brazil, the West African coast along the Gulf of Guinea, over some of the islands of Indonesia, and along the coast of southern China and Southeast Asia. The brighter surfaces, e.g., the Sahara, may have somewhat larger errors due to neglected viewing geometry dependence. The rapidly varying parts of the snow-covered land have an uncertainty in reflectances of $\approx 10\%$. The error caused by the failure to remove ozone absorption effects is only significant at higher latitudes for brighter surfaces (see Matthews and Rossow 1987). Overall, the estimated errors in land reflectance are smaller than the effective VIS threshold used.

3) OCEAN SURFACE TEMPERATURE

Remote sensing of sea surface temperature (SST) has been studied since the first satellites began measurements of infrared radiation; several types of data and several analysis techniques are now used to retrieve SST with errors, for monthly means averaged over regions of ≈ 250–500 km, estimated to be ≤ 1 K (Njoku 1985). Most of the remaining uncertainty is produced by lack of accurate measurements of atmospheric water vapor abundance (e.g., Maul and Sidran 1973; Maul et al. 1978) and of accurate calibration of the radiometers, although there are some real differences between the "skin" temperature measured by satellites and the bulk temperature measured by ships (Barton 1985; McClain et al. 1985).

Our technique has been tested in several ways as shown in Table 3. The statistical tests (treating large regions of the ocean as homogeneous targets) reveal some regions in the tropics that exhibit cloud contamination; however, the magnitude of the temperature errors is only 2–3 K. Case studies confirm many details of our results, including specific anomalies occurring in 1977, which is an El Niño year (Miyakoda and Rosati 1982), and the magnitude of horizontal temperature gradients (see Ro89). Figure 6 summarizes the comparison of the monthly mean SR SST values with colocated monthly average ship observations by showing histograms of the differences for 1 deg square regions. The narrow distributions are consistent with the estimated radiometer noise, effects of water vapor variability (Maul et al. 1978), and estimated uncertainties in the ship data (Barnett 1984; Wright 1986). The Southern Hemisphere comparison (Fig. 6b) may indicate more than usual cloud contamination in our results, although ship data are very sparse.

The bias of 2–4 K does not affect the accuracy of the cloud detection because the radiances inferred from these SST values represent the effective values measured by the NOAA-5 SR and are used directly in the cloud analysis. Part of the bias can be accounted for by two effects that have not been included in our radiative model (see Ro89). Correcting the assumed surface emissivity ($=1$) to estimates of the actual emissivity of water would decrease the bias by about 1 K. Correcting the water vapor absorption to account for the neglected weak absorption lines (Grassl 1974; Barton 1983) would decrease the bias by about 1–2 K in the tropics; at other latitudes the bias and this correction are smaller. The seasonal variation in the bias, shown in Fig. 6, is attributed to this same water vapor error. The rest of the bias can be explained by the difference between the radiometer "skin" temperature and the subsurface ship measurement, which can be as large as 1 K in the open ocean (Bernstein 1982; Barton 1983), and the uncertainty in the calibration of the radiometer, which could account for as much as 2 K of bias.

Sea ice positions compare favorably with other analyses (as discussed above), but no information is available to verify the surface temperatures retrieved. Since water vapor abundances are very low, the expected error that would affect cloud detection is caused by any variability on time scales shorter than 1 month, which is neglected in this analysis, and cloud contamination.

In summary (see Ro89), the uncertainty in the relative SST values (with the bias eliminated), is ≈ 2–3 K, associated with radiometer noise and uncertainties in atmospheric temperature and water vapor abundances. Comparisons of other SST climatologies have shown rms differences of about 1 K *when averaged over larger regions* (Reynolds 1983). Variations of sea ice surface temperatures are not well studied, but we estimate from small-scale spatial variations that the uncertainty is about ≈ 3–4 K. Overall, the estimated

errors in ocean surface temperature are smaller than the effective IR threshold used.

4) LAND SURFACE TEMPERATURE

Land surface temperatures are more variable because of the faster thermal response of the land surface to diurnal, synoptic, and seasonal variations of solar insolation. The result of our satellite data analysis is assumed to represent the monthly mean surface temperature *at the local time of day corresponding to the satellite overflight.* This result is then combined with the day-to-day deviations from the monthly mean (assumed constant over 250 km) inferred from the NMC analysis data to produce a daily surface temperature value at each location at a spatial resolution of about 25 km.

Figure 7 shows the histogram of the differences between the monthly mean satellite values and monthly mean, colocated surface station reports[9] averaged over 1 deg square regions. The distribution of differences is much broader over land, $\approx$5–7 K, than for the ocean surface. However, the geographic variation of land surface emissivity, especially that associated with vegetation and moisture variations, increases the dispersion of the differences between the blackbody temperature and the actual surface temperature. Since the surface temperatures (clear radiances) are determined individually for each location, assuming that the emissivity is 1, actual variations of surface emissivity do not affect the reconstruction of the clear scene IR radiance as long as the surface temperature used is obtained for the same location. Thus, the differences shown in Fig. 7 probably overestimate the actual error in the clear scene radiances by 1–2 K.

The bias shown in Fig. 7 is also larger and more variable with season than for the ocean surface. The same factors contribute to the land bias as for the ocean (see Ro89), with the water vapor effect slightly smaller[10] and the emissivity effect larger, $\approx$2 K. The equivalent of the skin temperature effect for land measurements is that the solid surface or vegetation canopy "skin" temperature differs from the air temperature at 1–2 m altitude where it is measured by weather stations. This difference can be quite large and varies with season and time of day (Minnis and Harrison 1984a,b).

Several case studies were performed (see Table 3 and Ro89) to test the ability of the combination of SR and NMC data to reproduce the day-to-day surface temperature variations. The station temperatures in cloudy regions were found to be warmer (colder) than the satellite temperatures in winter (summer), while adjacent clear regions were in good agreement. This effect is produced by the difference in the samples of time variations included in the two monthly averages: whereas the station data include measurements from every day in the month, cloudy or clear, the satellite data only include measurements for clear days. The radiative effect of cloudiness on land surface temperature is not included in the retrieved values. The effect of this discrepancy on the cloud detection is small because the errors are largest under the cloud cover.

In summary, the dispersion of the temperature differences and the discrepancies shown in the test cases suggest that our analysis method reconstructs land surface temperatures within about 5–8 K. These errors are smaller than the effective IR threshold used.

b. Threshold sensitivity tests

Errors in the deduced surface properties or radiative model assumptions can produce spurious nonzero values of TAU and ZC in a clear scene when the "noisy" satellite-measured radiances are compared to "imperfect" model radiances. Since actual values of TAU and ZC can be arbitrarily small,[11] "real" values may be confused with these (generally) small spurious values. This problem is exacerbated by partial cloud cover in the radiometer FOV which can decrease the contrast between clear and cloudy radiances, especially when the cloud cover fraction of the FOV is very small (see discussions in Rossow et al. 1985). To prevent spurious cloud detections and to compensate the derived cloud amount (partially) for the FOV problem, TAU and ZC are required to exceed some "threshold" magnitude before a pixel is labeled as cloudy. The interpretation of this procedure is that clouds are not considered present unless the detection "signal" (difference between the observed radiance and the model radiance predicted for clear sky) is greater than the "noise" (errors in the derived surface properties, in other data put into the model calculation, in model assumptions, and real noise in the radiance measurements). This approach provides an instrument and resolution dependent definition of "cloud" in terms of the magnitude

[9] This dataset is obtained from the NMC reports of conventional weather station surface temperature measurements for the time closest to the satellite overpass time. Differences in time of up to 2 h still exist, contributing to some of the difference shown in Fig. 7. Although these same data are used to produce the NMC analysis of surface temperature, there are significant differences between the station report summary and the NMC analysis product, which also contribute to the differences shown in Fig. 7. In addition to the differences illustrated in Fig. 2, the NMC analysis takes no account of the time of day.

[10] Daytime relative humidities are lower over land than ocean because the larger diurnal temperature variations on land produce colder temperatures at night that constrain water vapor abundance; available moisture for evaporation is also limited.

[11] In fact the atmosphere is never completely free of aerosol; however, our use of the average satellite-measured surface properties includes the mean aerosol effect in the "clear" scene radiances, so that only variations of background aerosol would be detected as cloud.

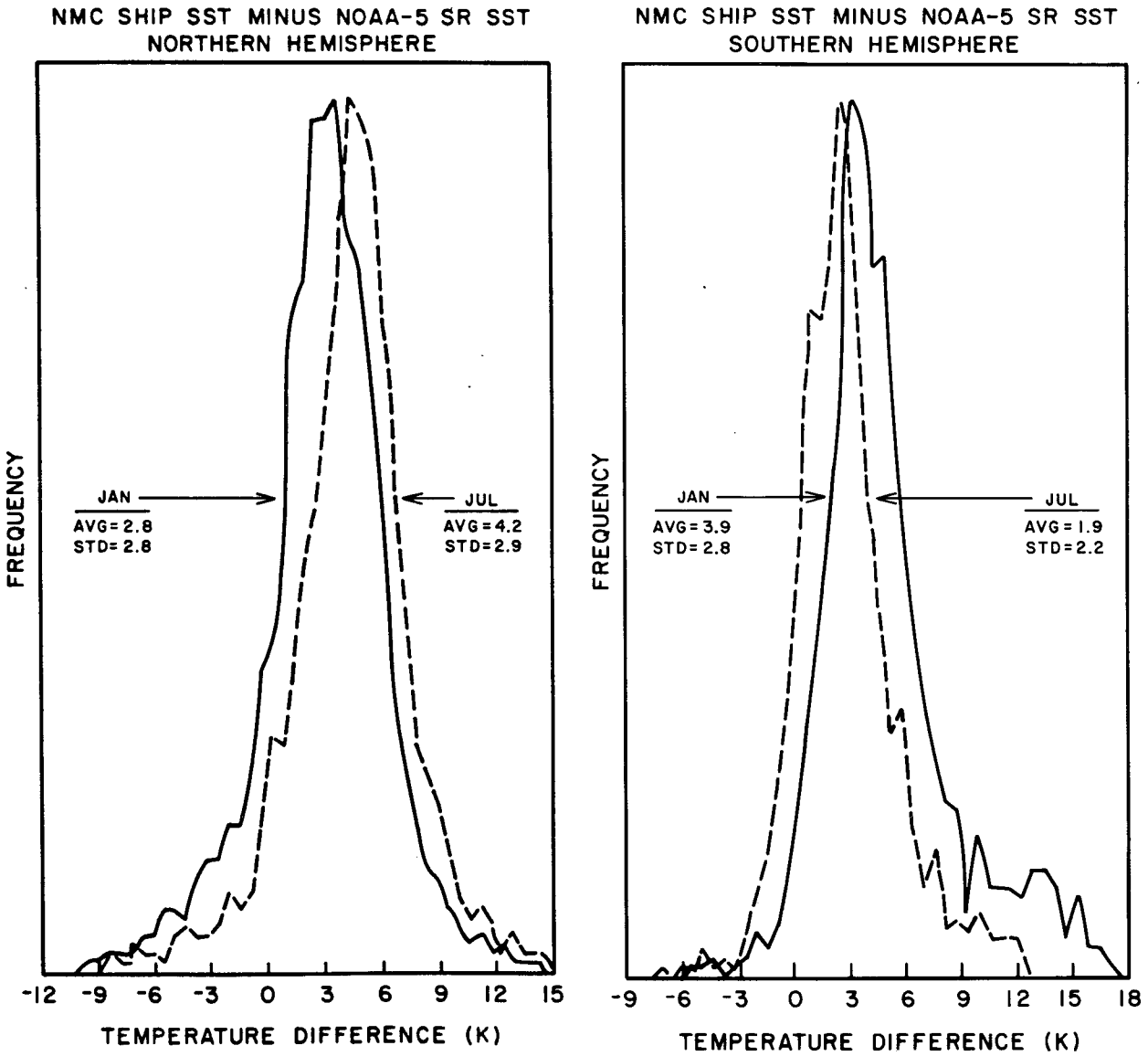

FIG. 6. Distribution of the differences between the monthly mean sea surface temperatures from the NMC ship data and the NOAA-5 SR analysis for January (solid) and July (dashed) 1977 in (a) the Northern Hemisphere and (b) the Southern Hemisphere. The average difference and the standard deviation of the differences are also shown.

of a cloud's effect on the particular satellite-measured radiances: in this case, *a cloud is that variation in atmospheric optical properties large enough to produce a measurable variation of the VIS and IR radiances over an area of* $\approx$8 km $\times$ 8 km. The studies summarized in section 4a were used to determine the effective noise level in the analysis. Here we describe several sensitivity tests conducted to select the "best" threshold values and logic and to determine the rate of change of cloud amount with variations of these threshold values. The sensitivity of this analysis method was also evaluated in studies conducted as part of the ISCCP cloud algorithm intercomparison study (Rossow et al. 1985).

Threshold "logic" refers to the decision logic used to detect clouds: with two radiance measurements available for each location there are several possibilities. The nature of the problem (see also Rossow et al. 1985) is illustrated in Fig. 8, which shows radiance relationships characteristic of four partially cloudy situations. The first panel shows radiances for midlatitude synoptic scale cloudiness over ocean, including a mixture of broken cumulus and stratus clouds. The clouds generally produce distinct changes from the surface (clear sky) values in both spectral channels. The second panel shows the measurements for broken, marine boundary-layer stratocumulus clouds; the cloudy radiances are

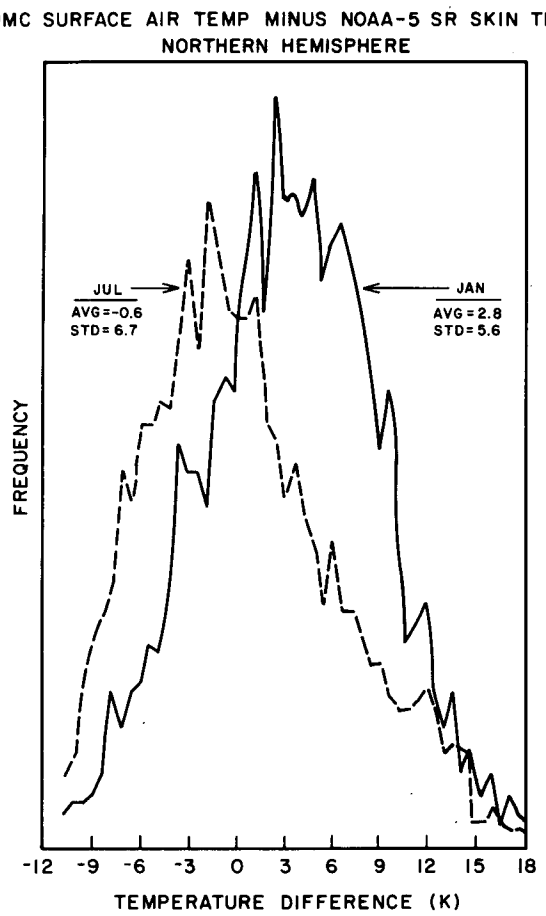

FIG. 7. Distribution of the differences between the monthly mean NMC surface station air temperature reports and the NOAA-5 SR "skin" temperature for January (solid) and July (dashed) 1977 on the Northern Hemisphere land surfaces. Only the station report nearest in time to the NOAA-5 overflight time is used in the average. The average difference and the standard deviation of the differences are also shown.

distinct only in the visible channel. Some of the cirrus clouds over ocean shown in the fourth panel, on the other hand, are distinct only in the IR channel. In other words, some cloud types are hard to detect in one or the other of the spectral channels employed here (see also, Saunders 1986), which argues for a decision logic in which a detection in either channel is accepted (cf. Shenk and Salomonson 1972b). The third panel provides an argument against this logic: this scene is a mixture of cloud, winter land with snow covering a complex of forest and fields, and partially ice covered lakes. The usual trend of radiances from warm and dark (clear) to cold and bright (cloudy) is reversed in this case. Our algorithm was successful in this situation because the clouds represented a correlated change of radiances (increased VIS and decreased IR) away from the particular clear sky conditions at each location in the scene. Other locations with more surface variation produce poorer results. The general success of the clear scene analysis depends on the low correlation of the VIS and IR radiance variations in clear regions (cf. Sèze and Rossow 1989). Verification of that success (discussed in section 4a) suggests using a threshold logic that requires a correlation of the radiances for cloudy scenes, i.e., requiring a detection in both the VIS and the IR channels.

The discussion in section 4a (also Ro89) indicates the estimated errors in surface reflectivity and temperature; these global estimates are conservative in order to include some regions with larger errors. The magnitude of these radiance uncertainties is equivalent to uncertainties in TAU $\approx$ 1.0 and ZC $\approx$ 1.0 km away from their zero values. By comparing six daily global retrievals from January and July, using various values of the TAU and ZC threshold values and the two possible logical combinations, we tested the sensitivity of the cloud detection. These tests suggested that better results are obtained by requiring both TAU $\geqslant$ 1.2 and ZC $>$ 1.4 km for cloud detection (see below). Some specific reasons are 1) small errors in model ocean reflectivity lead to spurious, small TAU values; the ZC threshold is important in reducing this contribution to the total, even though some actual low clouds are also rejected; 2) errors in the variable snow and ice reflectivities are partially compensated by the ZC threshold, since surface temperatures seem less variable than surface reflectances in these locations; 3) errors in land surface temperatures, especially in mountainous terrains, are partially compensated by the TAU threshold. We selected this two-channel approach for its overall performance globally, even though some cirrus and low, broken cloud are excluded from the results.

We also compared the performance of this algorithm, using smaller threshold values (TAU $\geqslant$ 0.8 and ZC $\geqslant$ 0.5 km), with six other cloud algorithms in the ISCCP intercomparison study (Rossow et al. 1985). Overall agreement among the algorithms was estimated to be about $\pm$7% rms; spatial correlations were $>$0.7. However, specific situations showed worse agreement; differences for snow-covered land or tradewind cumulus regions were as large as 20%–40%. Our method obtained results in this test that were generally near the average of all the results. The primary deficiencies of this algorithm revealed in those tests were that some of the low-level, highly broken cloudiness over the subtropical oceans was missed because of the ZC threshold (even as small as 0.5 km) and some of the tropical cirrus was missed because of the TAU threshold (Rossow et al. 1985). Reliable detection of these "marginal" cloud types requires a better analysis to obtain more accurate clear sky radiances at both wavelengths.

The overall sensitivity of our cloud detection results (expressed as cloud amount) can be summarized in two ways. First, in Fig. 9, we show which parts of the global distribution of TAU (ZC) are rejected by various

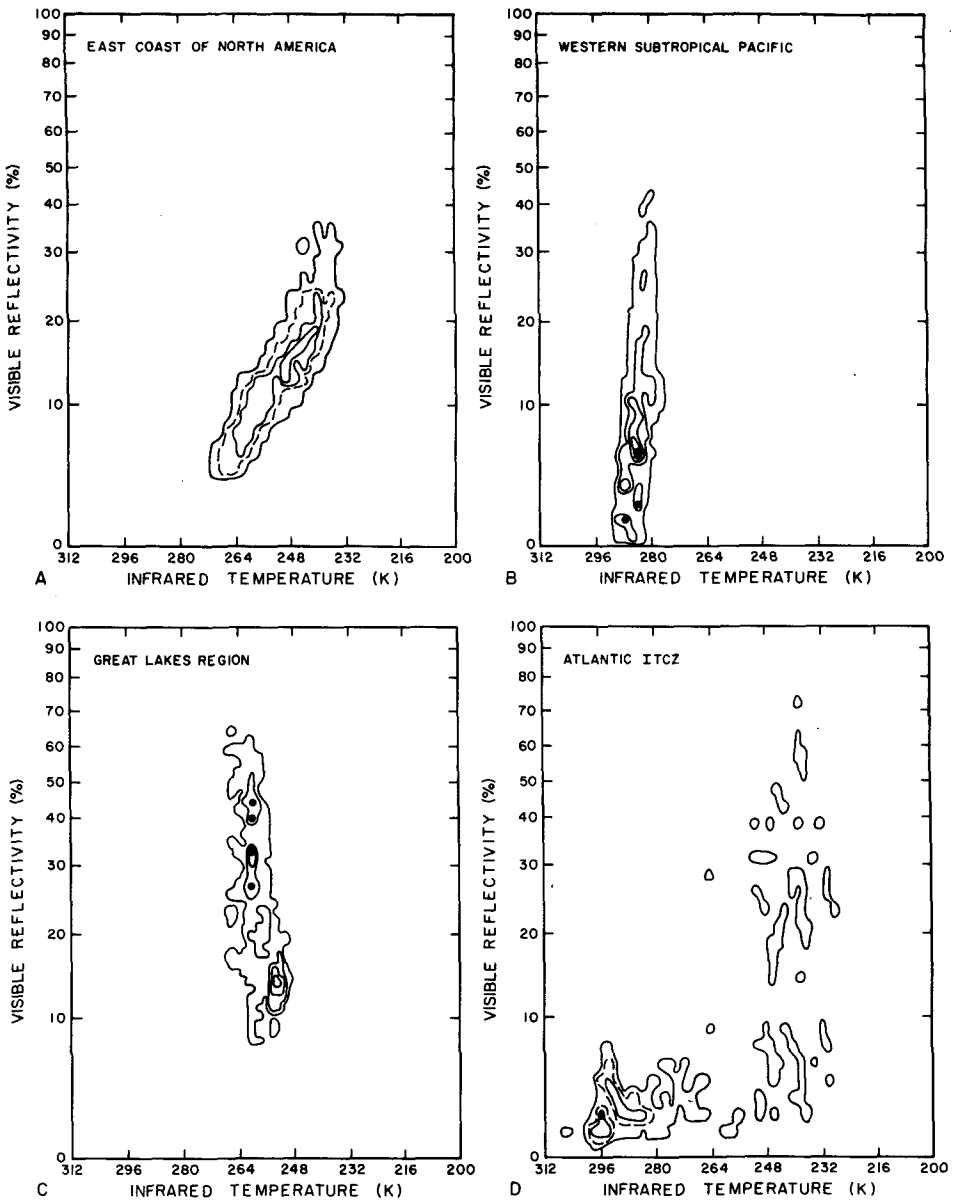

FIG. 8. Distributions of VIS and IR radiances for different cloud types illustrating the need for different cloud detection logics: (a) midlatitude synoptic-scale cloudiness that is easily detected in either spectral channel; (b) broken, marine boundary layer cloudiness that is more easily detected in the VIS channel; (c) winter stratus partially covering a surface composed of partially ice-covered lakes and partially snow-covered fields and forests that is difficult to detect in either spectral channel; and (d) tropical cirrus that is more easily detected in the IR channel.

values of the ZC (TAU) threshold. Figure 9a shows the total distribution of TAU values, including zero, obtained over the whole globe for 6 days in January and July. The distribution is partitioned into portions representing those TAU values corresponding to ZC values in the ranges, ZC = 0 (grey shading), $0 < ZC < 5$ (striped shading), $5 \leq ZC < 15$ (clear region to the left of the indicated line), and $15 \leq ZC$ (remainder of the distribution). Figure 9b shows the ZC distribution partitioned by the associated TAU values in the ranges, TAU = 0 (grey shading), $0 < TAU \leq 1$ (striped shading), $1 < TAU \leq 2$ (clear region to the left of the indicated line), and $2 < TAU$ (remainder of the distribution). (Note that all values mentioned in this paragraph and shown in Fig. 9 are coded values; see the figure caption.)

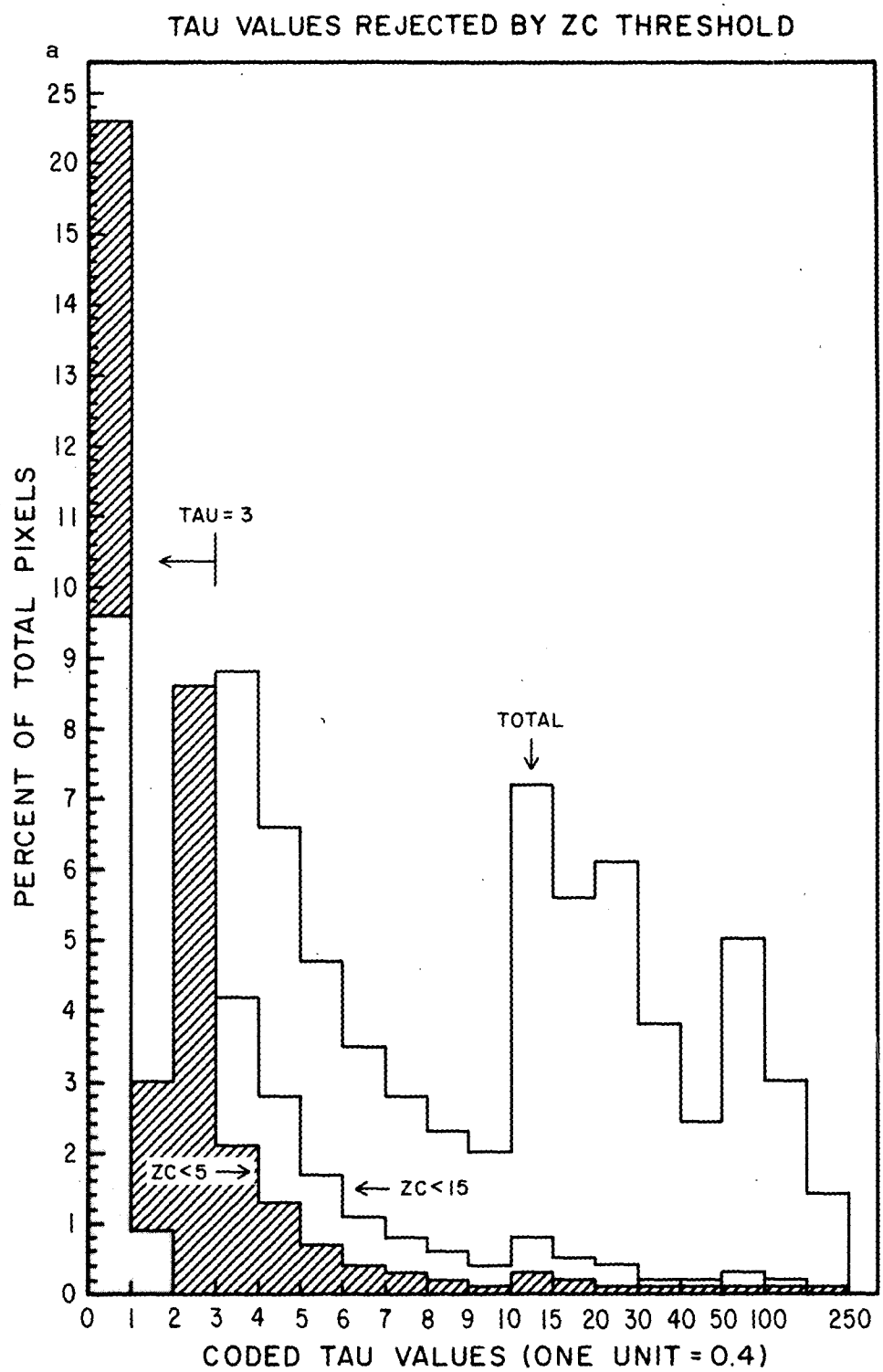

FIG. 9. Distribution of (a) TAU values showing those rejected by various ZC thresholds and (b) ZC values showing those rejected by various TAU threshold values. In each panel the total distribution of TAU or ZC is shown (including zero values). Note the interval changes along the abscissa. The portions of the total distribution associated with three ranges of the threshold parameter are indicated by shading and are described in the text. (The grey shading indicates the TAU/ZC values associated with a zero value of the other parameter.) The final thresholds for TAU and ZC are also indicated by arrows on the respective panels.

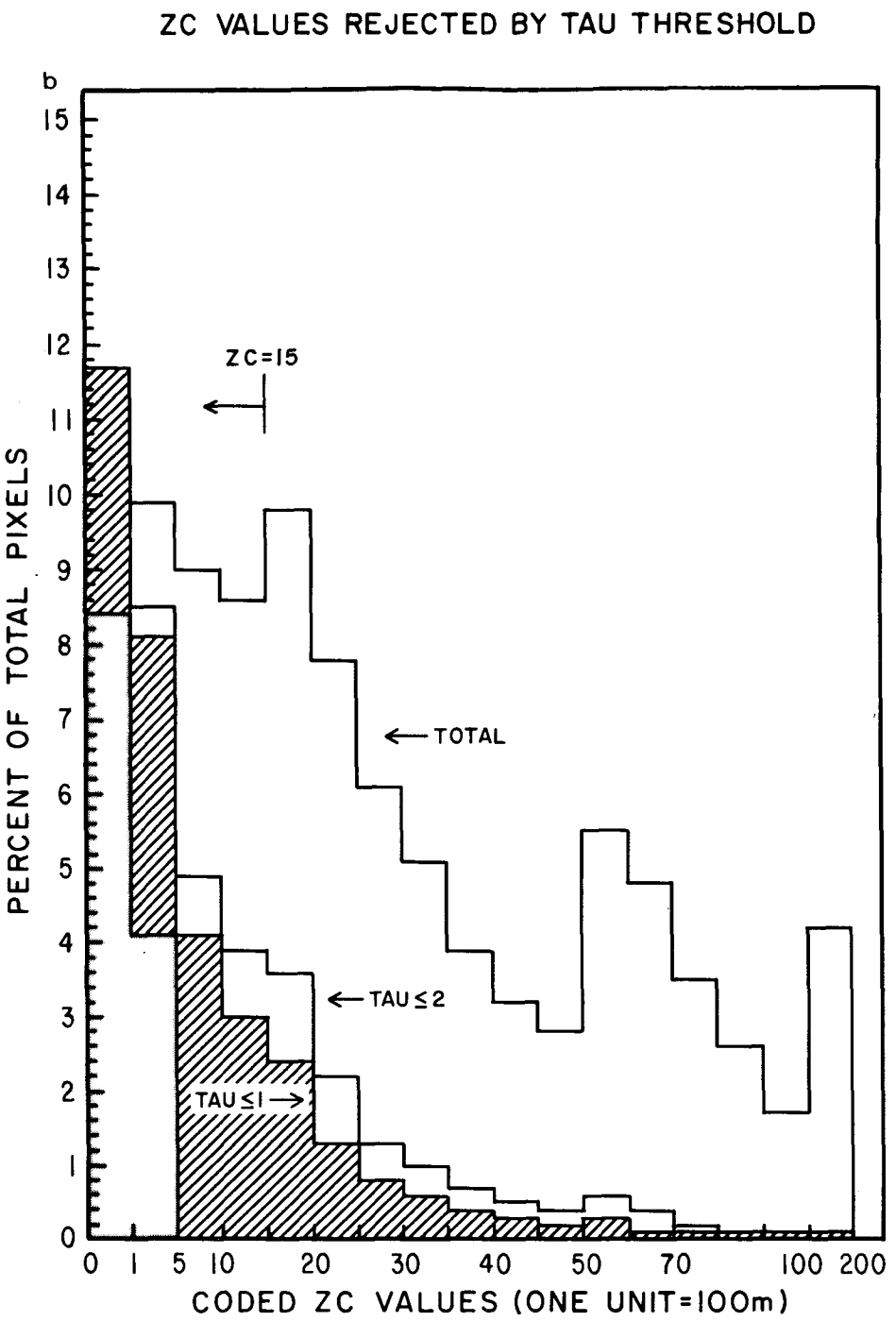

FIG. 9. (*Continued*)

As expected, smaller thresholds detect more "cloud." The correlation between TAU and ZC assumed in the analysis is demonstrated in Fig. 9 by the fact that the independent thresholds generally reject the smallest values of the other quantity. Most of the zero values of TAU and ZC are associated with each other; that some zero values are not is to be expected in a "noisy" system. The magnitude of the TAU and ZC thresholds needed to reject the remaining zero values of ZC and TAU, respectively, are TAU ≤ 0.4 (code value 1) and ZC < 0.5 km (code value 5); these values are consistent with, but smaller than the estimated uncertainties ob-

tained from the surface validation studies. Figure 9 also shows, however, that even these small threshold values reject some relatively high, thin cloud (large ZC and low TAU) and optically thick, low cloud (large TAU and small ZC) by requiring "detection" in both spectral channels; i.e., some types of cloudiness are more easily detected in one spectral region than another.

Examination of the specific cases, particularly time variations and motions of the "clouds" associated with the smaller values of TAU and ZC, suggests that the somewhat larger threshold values that we selected are required to eliminate spurious clouds produced by errors in the ocean reflectance model, in surface reflectances over snow and sea ice, and in the surface temperatures over higher topography. These larger thresholds also reject more "real" cloudiness (Fig. 9). The global and annual mean cloud amount determined with the final threshold values is 52.8%; if the smaller thresholds, just sufficient to eliminate all zero values of either TAU or ZC, are used, the global annual mean cloud amount would be increased by about 10%–15%, based on the analysis of the 12 days used in the case studies. In Fig. 9a, the break in the distribution near zero suggests a real separation of the clear and cloudy conditions in the VIS; however, in 9b, there is no such break. As Fig. 3 shows, the VIS/IR radiance distributions are continuous. Since some of the "clouds" obtained with these smaller values of TAU and ZC are spurious, based on the estimated errors in the clear scene radiances, this sensitivity of the global cloud amount suggests a cloud detection uncertainty of about ±5%–10%.

Although the particular choice of threshold logic and magnitude does not change the total cloud amount drastically, it does reduce the sensitivity of the analysis to two specific types of clouds: cirrus (very low TAU but high ZC) and boundary-layer clouds (very low ZC but high TAU). Although the most extreme of these cloud types appear to represent only about 10%–15% of the global total cloudiness, they may contribute significantly to the total cloud-radiative feedback (see Part II).

The second summary of the detection sensitivity is provided by counting the number of image pixels with TAU and/or ZC values near the threshold values, namely those pixels with either $1.2 < \text{TAU} < 2.8$ or $1.4 < \text{ZC} < 3.0$ km. Figure 10 shows the annual mean map of this quantity (δCC) (shown as a cloud amount). Wherever this number is larger, generally because of the presence of broken clouds, small changes in the

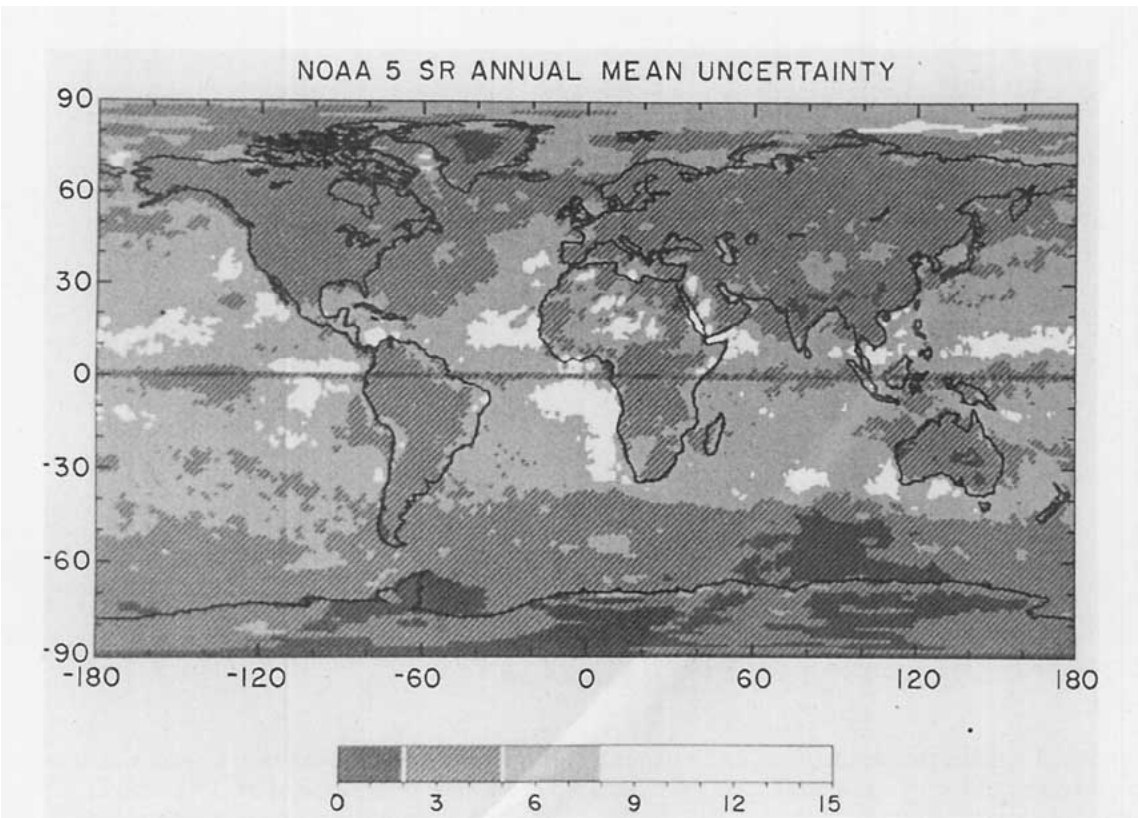

FIG. 10. Global distribution of the annual mean value of δCC; δCC is the average number of image pixels, expressed as a cloud fraction, with radiance values near the threshold values: either $1.2 < \text{TAU} < 2.8$ or $1.4 < \text{ZC} < 3.0$ km. The cross hatching indicates regions with δCC values below the annual global mean value.

TABLE 4. Summary of visible band radiance model sensitivity tests.

Quantity/feature tested	Test	Estimated TAU uncertainty (%)
Monochromatic approximation	Compare to explicit bandpass simulation	2
Order of polynomial expression	Increase order	5
Interpolation interval	Halve intervals	<5
Radiance noise	Vary input radiance	2
Surface pressure	Vary ±50 mb	<1
Ozone abundance	Vary ±20%[a]	5
Surface reflectance	Vary reflectance ± 5%[b]	<5
Cloud top pressure	Vary ±200 mb	<2
Tropospheric aerosol variation	Add aerosol[c]	<2
Surface angular dependence	Vary reflectance ± 5%[d]	<5
Cloud droplet size	Vary from 5–20 μm	15
Estimated total		15–20

[a] Ozone uncertainty estimates from Hilsenrath et al. (1979); variability estimates from Bowman and Krueger (1985).
[b] Uncertainty estimates based also on results of Matthews and Rossow (1987).
[c] Aerosol properties and distribution from Toon and Pollack (1976).
[d] Angular variation estimates from Kimes (1983).

selected threshold values would produce larger changes in the detected cloud amount; i.e., the cloud amount is more uncertain in such a case. Figure 10 shows that the value of δCC is generally ≤5%, with the larger (≈7%–15%) uncertainties associated mostly with the oceanic subtropical regions that are dominated by broken, boundary-layer clouds. The global mean value of δCC is 5%; i.e., the global cloud amount would be reduced by about 5% if the threshold were doubled. This result is consistent with the sensitivity illustrated in Fig. 9, suggesting an uncertainty in the detected cloud amount of about ±5%, averaged over the globe, with somewhat larger regional uncertainties which approach ±10%–20%. We emphasize that this estimate refers to the uncertainty in the count of cloudy pixels; the actual cloud amount depends on the magnitude of the effect of partial coverage of the NOAA-5 SR FOV (see section 4d).

c. *Radiance model sensitivity tests*

The accuracy of the narrowband radiances simulated by the models used for this study depends on the magnitude of four types of uncertainties: 1) model shortcuts or approximations to decrease computational load, 2) uncertainties in measurements of atmospheric or surface properties used in the calculation, 3) effects of the atmosphere or surface on radiances that are neglected in the models, and 4) effects of clouds on radiances that are neglected in the models. The second type of uncertainty is produced directly by measurement errors in the input data. The last two types are caused by the model representations of atmosphere, surface, and cloud radiative effects which may not account correctly for all aspects of these phenomena. The sensitivity tests performed to study these uncertainties are summarized in Tables 4 and 5 and all tests are a repetition of a global analysis of 6 days of data in January and July after changing or varying the specific model aspect indicated. The tables show the overall magnitude of variations in the retrieved values of TAU and ZC. All estimates in Tables 4 and 5 represent the uncertainty in single retrievals; uncertainties in

TABLE 5. Summary of infrared band radiance model sensitivity tests.

Quantity/feature tested	Test	Estimated ZC uncertainty (m)
Monochromatic approximation	Compare to explicit bandpass simulation	<150
Finite layer thickness	Decrease layer thickness	<150
Surface humidity approximation	Use full model	150
Thin cloud formulation	Use full model	500
Angle interpolation	Use full model	<300
Radiance noise	Vary input radiance	300
Atmospheric temperature	Vary ±3K[a]	500
Water abundance	Vary ±50%[b]	<150
Surface temperature	Vary ±10K	<300
Cloud optical thickness	Vary ±30%[c]	500
Water vapor absorption	Vary ±50%[d]	<300
Tropospheric aerosols	Add aerosol[e]	<150
Estimated total		500–1000

[a] Estimated uncertainty based on Smith et al. (1979).
[b] Estimated uncertainty from Rosen and Salstein (1980).
[c] For optically thin clouds only.
[d] Uncertainty estimated from study reported in section 4b.
[e] Aerosol properties and distribution from Toon and Pollack (1976).

monthly mean values due to these factors are smaller. The specific effects of these uncertainties on the cloud detection were discussed above.

Since most clouds are opaque and the atmosphere is nearly transparent at VIS and IR wavelengths, uncertainties in specifying or calculating the atmospheric and surface effects on the radiances have little effect on TAU and TC. The total errors associated with these factors are no more than 5% in TAU and 2–3 K in TC, equivalent to an error in ZC of 300 m. The largest single error in TAU associated with atmospheric or surface effects is about 3% caused by errors in specifying the monthly mean ozone abundance and by neglecting longitudinal and synoptic variations of its abundance. (Errors due to uncertainty in the absolute calibration of the VIS radiances may be as large as 10%–20%, however.)

The largest single source of error in ZC for opaque clouds, about 500 m, is associated with uncertainties in the atmospheric temperature measurements. However, this is mostly due to the direct error of specifying the temperature at a specific height, rather than in measuring TC. The neglect of the weak water vapor absorption lines in the 10–12 μm wavelength region in the IR model produces a significant underestimate of the atmospheric absorption (e.g., Grassl 1974; Cutten 1985), but this error affects the retrieved surface temperature (see Ro89) more than TC, because most of the water is below the cloud. The value of TC is insensitive to errors in the atmospheric properties; the largest source of error in TC is in the SR measurements, themselves (especially absolute calibration which is not considered in Table 5).

The TAU and ZC values for thinner clouds (TAU $\leq$ 2) are more sensitive to errors in the surface properties because the total scene radiances are partly determined by radiation from the surface that is transmitted through the cloud. The estimated uncertainties associated with surface properties for retrieval of thinner cloud properties are therefore somewhat larger than discussed above.

By far the largest general sources of error for TAU (Table 4) are associated with the radiative transfer model; interpolation errors can be as large as 10% at the more extreme viewing geometries, while the use of a constant cloud droplet size could produce errors up to 15% (see also, Arking and Childs 1985). In ice clouds the particles are not spherical, as assumed in this model, which can cause changes in the angular distribution of radiation scattered from a single particle (Stephens 1980; Asano and Sato 1980); however, the predominance of multiple-scattering for most clouds at visible wavelengths makes the value of TAU much less sensitive to particle shape than to effective size.

The TC and ZC values for thin clouds are more uncertain because they are sensitive to the assumed relation between the VIS and IR optical depths used in Eq. (6) to correct for the effects of decreased emissivity and increased transmissivity. This relation depends on the wavelength variation of the optical properties of water and ice (there has been some disagreement about the optical properties of ice; cf. Warren and Shettle 1986) and on the detailed size distribution and shape of ice particles. For water and ice spheres, Mie calculations can provide an accurate relation between the VIS and IR extinction optical depths (Hansen and Travis 1974; Arking and Childs 1985). However, use of the IR extinction optical depth in Eq. (6) overestimates the cloud effect by about 50% (cf., Stephens and Webster 1981) because the scattering at these wavelengths is mostly in the forward direction. Using the absorption optical depth is a better approximation for spherical particles (Platt and Stephens 1980). For lower altitude clouds (likely to be composed of liquid droplets) with smaller contrast between TS and TC, the correction obtained with Eq. (6) and our estimate of the extinction optical depth underestimates ZC by about 0.5–1 km. In ice clouds the nonspherical shapes of the particles alter the relation between the visible and IR optical depths significantly (Platt 1979; Stephens 1980; Asano and Sato 1980); in particular, the reduction of forward scattering increases the IR effect relative to the visible effect. Available measurements and estimates of this ratio (Platt and Stephens 1980; Stephens and Webster 1981) suggest that the error in ZC obtained with Eq. (6) may be 1–2 km.

In all these sensitivity tests our radiative transfer model assumes that cloud effects on satellite-measured radiances can be represented by a thin, homogeneous layer covering the SR FOV. The total uncertainty associated with the factors considered in Tables 4 and 5 is 15%–20% for TAU and 5%–10% for ZC. However, the neglect of actual small-scale inhomogeneities and vertical structures in clouds, including that represented by fractional cloud cover of the FOV, may represent the largest error in the retrieval of cloud properties, but there is currently no analysis method or theory that accounts for these effects in a practical way. Stephens (1988) discusses this issue more thoroughly and suggests some possible theoretical approaches to the problem (see also Rossow 1989). Estimates of the effects of some specific variations in cloud structure suggest that they could be important (McKee and Cox 1974; Davies 1978; Ellingson 1982; Harshvardhan and Weinman 1982a,b; McKee et al. 1983; Harshvardhan and Thomas 1984; Davies 1984; Welch and Wielicki 1984; Naber and Weinman 1984; Duvel and Kandel 1984), but there is no estimate of errors in calculated radiances using retrieved "effective" parameters like our TAU and TC values (see, e.g., Schmetz 1984, and discussion in Rossow 1989). Further studies with data containing more complete information about cloud structures and the radiation field in cloudy situations are required to assess this uncertainty (Cox et al. 1987).

The magnitude of the error caused by the overestimate of cloud amount in the SR FOV can be crudely estimated by determining the sensitivity of individual values of TAU and ZC to the fractional coverage assumed. This error is a bias error: cloud cover of the FOV less than 100% requires larger TAU and smaller TC (larger ZC) for the same VIS and IR values. For a change in the cloudy value of VIS of +20% (relative), equivalent to a reduction of the assumed FOV cloud amount from 100% to 80%, TAU varies by +20%–100% (relative); whereas a change in the cloudy value of IR of −20% (relative) represents variation of TC by −8–10 K or ZC by +1.5–2 km (cf., Arking and Childs 1985).

The magnitude of this error on the monthly mean results is not as large since the values most likely to be in error because of partial FOV coverage are the lower values of TAU and ZC. The effect on the global, monthly mean values produced by a 50% change in the assumed cloud amount for the lowest quartile of the TAU and ZC distributions is, in addition to an overall decrease of cloud amount by about 10%, an increase in the mean TAU of about 2 and an increase of the mean ZC of about 500 m. Regional values change by smaller or larger amounts (up to about 6 for TAU and 1200 m for ZC).

In summary, the largest source of uncertainties in the retrieved *homogeneous model* cloud properties is associated with the second factor listed at the beginning, namely, errors in the available information about the atmosphere and surface. Modeling the effects of the atmosphere and surface is not a serious constraint on accuracy; modeling of the surface effects is not as accurate as the atmospheric effects, but this could be improved by further analysis of the satellite data (see Ro89). The most serious source of uncertainty in *actual* cloud properties inferred from the model properties comes from the last factor, namely the representation of the cloud in the radiative transfer model. The results of our sensitivity tests confirm the first order importance of TAU and TC on the satellite-measured radiances and show that the particle properties of homogeneous clouds are the next most important parameters in the results (cf. Arking and Childs 1985), especially for thinner clouds. However, determining the proper treatment of the small (subpixel) scale inhomogeneities in the models remains the largest source of uncertainty in the interpretation of the satellite observations (Rossow 1989).

d. Comparison to other data

Some estimates of the magnitude of the effect of partial FOV coverage suggest that the cloud amounts obtained from "low" resolution data (4–10 km pixels) could be biased high by about 10%–20% (Young 1967; Shenk and Salomonson 1972a; Coakley and Bretherton 1982; Minnis and Harrison 1984a; Arking and Childs 1985; Rossow et al. 1985); however, in practice, the larger threshold used with low resolution data can (partially) offset this error (cf. Stowe 1984; Stowe et al. 1988). Rossow et al. (1985) conducted a sensitivity study with six different methods (including the one discussed in this paper) by varying the data resolution from 8–32 km; the change in cloud amount was only 5%–10% over this range of data resolutions. In section 4c we estimated the cloud amount error by counting *all* very low values of TAU ≤ 6 and ZC ≤ 2.0 km as 50% cloud covered FOVs; this change decreases the total global cloud amount by less than 10%. The geographic distribution of low TAU and ZC values is not uniform, however. In the marine stratus régime, the decrease is as large as about 20%. If all the pixels with radiances near the threshold (Fig. 10) are associated with FOV cloud amounts of zero, the global mean cloud cover is reduced by only 5%. All of these estimates suggest a cloud amount uncertainty of 5%–15%.

The only other available way to obtain an overall assessment of the net effect on the cloud cover determined in our analysis of all the factors discussed in section 4c is to compare our cloud amount with other analyses of cloud observations that have different data resolutions and analysis methods. Figure 11 shows the zonal mean cloud amounts for January and July 1977, obtained from the NOAA-5 SR analysis, compared with those from several other global cloud climatologies that are averaged over a variety of time periods. The bars on our results represent plus and minus the zonal mean values of δCC (Fig. 10). The other climatologies represent observations from the surface (London 1957), other satellite analyses (Arking 1964; Miller and Feddes 1971; Henderson-Sellers 1986), and combinations of these two (Schutz and Gates 1971; Berlyand and Strokina 1980). The comparison shown in Fig. 11 is generally favorable to our results, showing agreement with the other climatologies to within $\pm 10\%$ generally, and does not suggest any large (>20%) overestimate of cloud amount.

Although the cloud amount obtained is not significantly higher than obtained in other studies, this may result from offsetting errors: overestimation of broken cloud amounts and failure to detect very low level and cirrus clouds. The amount of cirrus and low-level clouds missed because of the thresholds employed could contribute as much as 10%–15% to the global total, based on the results shown in Fig. 9. The possibility that much of the low-level cloudiness missed by our thresholds is the same type of cloudiness for which overestimation errors are largest complicates the assessment of this source of error.

Several significant differences do appear in Fig. 11 that suggest areas for further improvement. The two largest differences in January zonal mean cloudiness (Fig. 11a) are in northern midlatitudes and subtropics.

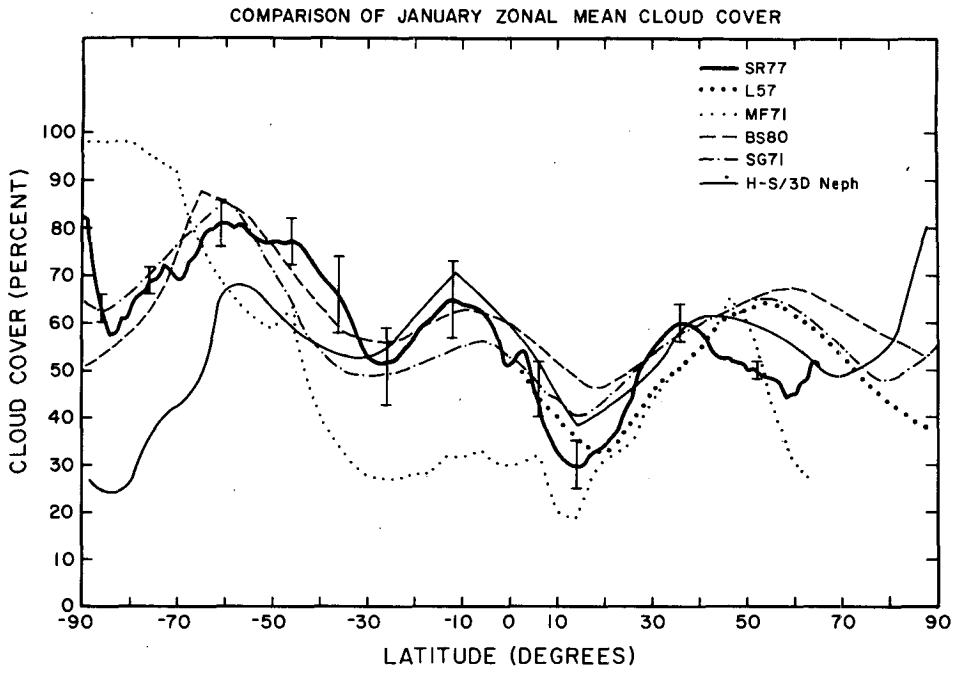

FIG. 11. Comparison of zonal mean CC for (a) January and (b) July from NOAA-5 SR results and other climatologies: London (1957), Miller and Feddes (1971), Berlyand and Strokina (1980), Schutz and Gates (1971), Henderson-Sellers (1986), and Arking (1964). Error bars represent ± (zonal mean) δCC from Fig. 10.

The first difference may indicate a problem in satellite detection of low clouds over snow-covered land (as discussed in sections 4a), because the deviation between our results and the others begins near the zonal mean snow line. This discrepancy also coincides with the oceanic storm tracks and may also indicate missed low-level clouds over ocean. This latter effect may also explain the similar, but smaller, difference in the subtropics. A similar difference is also apparent in northern midlatitudes in July, so that some of the discrepancy may be due to real time variations. In particular, since our data represent morning observations, the generally lower cloud amounts over land in our results may be part of a diurnal variation (cf. Minnis and Harrison 1984b).

The differences in the amount of cloud determined for the northern subtropics in January (and possibly the northern and southern subtropics in July) may be the result of the ZC threshold that rejects IR radiances that are within about 9 K of the clear scene radiance. Some of the low-level, broken boundary layer cloudiness, characteristic of the tradewind regime in the subtropics, is missed by this low sensitivity threshold, although low-resolution satellite data also tends to overestimate the amount of this type of cloud (cf. Minnis and Harrison 1984a; Rossow et al. 1985). A similar problem occurs in the marine stratus regime in the same latitude zone (cf. Coakley and Bretherton 1982; Minnis and Harrison 1984a). Some of the difference at this latitude can also be caused by differences in the longitudinal sampling in the climatologies, since the very low cloud amounts over subtropical deserts are partially offset in our zonal average by the much higher cloud amounts over the subtropical oceans associated with the marine stratus regimes. Satellite observations may provide a more complete sample of clouds at these latitudes (cf. London and the satellite cloud climatologies in Fig. 11).

The largest differences in July (Fig. 11b) are in the north polar and southern middle to high latitudes. Both polar regions show large disagreements among these cloud climatologies. Our results happen to agree with some of the other climatologies near the south pole, but show larger discrepancies near the north pole. The difficulties in describing the clear scene radiances (surface properties) in these regions (see section 4a and Ro89) may make our results unreliable in both regions, but the comparison to other results does not provide a useful assessment of our method.

The downturn in CC at southern middle to high latitudes is related to the difficulty in distinguishing sea ice and cloud in this region at low illuminations (see section 4a). The large disagreement between the IR-based satellite result (Henderson-Sellers 1986) and the VIS-based result (Miller and Feddes 1971) at these latitudes may also be caused by a larger abundance of

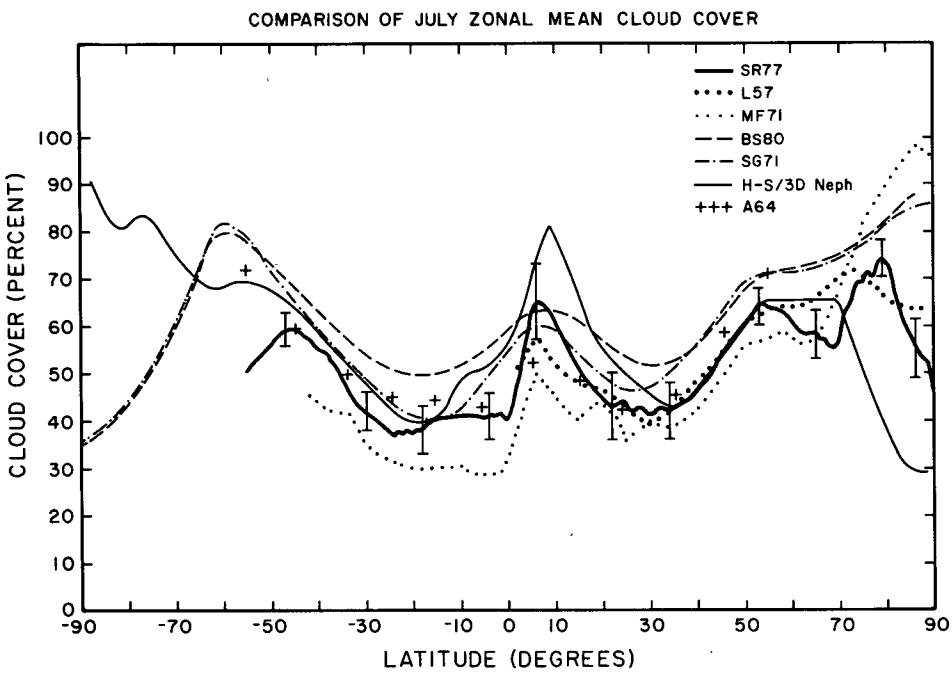

FIG. 11. (*Continued*)

thinner clouds in this region as our results suggest (see Part II), since the Miller and Feddes (1971) analysis associates low cloud amount with low reflectances.

The large differences among all the climatologies that occur in the ITCZ may be caused by differences in the latitudinal resolution of the climatologies, in addition to differences in longitudinal sampling, since the ITCZ appears to be a very narrow feature with strong latitudinal and longitudinal variations (see Part II). Some of the difference may also be due to the rejection of some very low TAU "clouds" (namely, cirrus) in our results, which would serve to decrease the total cloud amount and reduce the apparent latitudinal width of the ITCZ (see Part II). This effect would also explain the relation between our results and the three-dimensional nephanalysis results, which rely exclusively on measured IR. Since the results of Miller and Feddes (1971) rely on the magnitude of VIS to estimate cloud amount, the predominance of thinner (i.e., "darker") clouds in the ITCZ also causes an underestimate of the cloud amount.

The differences in the "operational" definition of cloud amount used in various cloud climatologies can account for large differences in their values. Also, these climatologies represent averages over different time periods which can represent actual variations in cloud amount. Thus, the differences apparent in Fig. 11 cannot be uniquely explained. We conclude that these climatologies can provide no more constraint on estimates of the accuracy of our results than the other estimates already presented. Note, for example, that the multiyear climatology of London (1957) based on surface observations agrees well with the earliest 1-yr satellite climatology of Arking (1964); there is no way to evaluate which of these results is the most reliable. Demonstrating a higher accuracy for future cloud climatologies will require more definitive procedures to validate the results, including better understanding of the data characteristics, comprehensive assessments of the sensitivity of the analysis algorithm, and detailed intercomparisons with special intensive cloud observations. This is the plan for ISCCP (Schiffer and Rossow 1983).

Few systematic surveys of the other cloud properties exist, but verification of other cloud properties by comparison to available results is also made difficult by the variation of definitions used. For example, earlier cloud climatologies contain information on cloud heights (usually base heights), but this is reported as cloud amounts in three height categories, often assuming some relation between the cloud amount observed directly and cloud amount obscured by intervening clouds. Since different assumptions regarding this "overlap" are used to process the observations, the average cloud height corresponding to that directly observed by satellite cannot be reconstructed. Henderson-Sellers (1986) compares results from the Air Force 3-D Nephanalysis to those of London (1957). Based on the 3-D nephanalysis values we can estimate a global mean ZC of 3.5–5.5 km, depending on the overlap

assumed. This result is consistent with our result, but not especially restrictive. In Part II, we examine such comparisons further.

5. Conclusions

These results have illustrated several positive aspects of this type of analysis of satellite data. The first is that the use of the same data to infer both clear and cloudy scene radiances better isolates the cloud effects without need for detailed modeling of surface radiative properties. Several characteristics of other, more conventional, surface data cause too many interpretation uncertainties when used with satellite data (see Ro89). In addition, available surface observations do not have complete global coverage at sufficiently high resolution to show all of the detail seen in the satellite clear scene radiances. There was a clear improvement in our results using the satellite-based surface properties in place of the conventional data. Although there are still some problems with correctly identifying clear scene radiances from satellite data (see below), pursuing this approach seems more likely to obtain the most reliable specification of the clear radiance values. With better clear scene radiances, the sensitivity of cloud detection can be increased without creating too many spurious detections. This is a crucial improvement needed to improve the analysis of cirrus and boundary layer cloudiness in particular (cf. Rossow et al. 1985). This increased sensitivity is also important to improved cloud analysis in the polar regions, where cloudy and clear radiance contrasts can be very low.

The particular cloud algorithm presented here still has several shortcomings, some of which indicate fundamental limitations on the accuracy of cloud observations derived from this type of satellite data. These problems are caused by persistent cloudiness and highly variable surface properties. The first problem makes identification of clear radiance values difficult simply because very few actual measurements are possible in extremely cloudy locations. If the clouds persist over long periods, greater than 1 month, determinations of clear scene radiances that rely on the variation of cloudiness with time cannot succeed. If such "cloud contamination" is not properly removed from the clear sky values [see Ro89 and Matthews and Rossow (1987)], the cloud amount will be underestimated and incorrect cloud and surface optical properties will be inferred. In some cases the clouds are sufficiently variable that our analysis method "recognizes" their presence even though it fails to obtain a reliable clear scene radiance; however, some types of persistent cloudiness resemble the variation statistics of clear scenes and are mistaken as clear (e.g., Fig. 3e). This problem seems to occur primarily over tropical land areas and subtropical oceans, but it may also be a problem in the polar regions. Improving the results in either case requires some new strategy to obtain a better measure of the clear radiances.

The second problem is the reverse of the first, where instead of clouds "masquerading" as clear scenes, the surface properties are so much more variable that they become confused with clouds. This problem occurs mostly in the vicinity of the snow and sea ice edges; however, mountainous terrain may also cause this type of confusion.

Many analysis techniques have been developed for the study of different types of clouds in different situations (see Table 1). Each of these algorithms exploits one or more characteristic difference between the spectral, spatial, and temporal behavior of cloudy and clear scene radiances, but these results have not been extended to all climate regimes. In our study we have illustrated some particular types of compensation in the cloud detection from the use of two spectral channels, where errors in one channel are sometimes offset by the other channel.

The first key result of this work is demonstration of the value of time-homogeneity tests to recognize clear scenes (see also, Sèze and Desbois 1987; Sèze and Rossow 1989), complementary to studies of spatial homogeneity (cf. Coakley and Bretherton 1982; Desbois et al. 1982). Our results and those of other studies (cf. Rossow et al. 1985; Saunders, 1986; Minnis et al. 1987) suggest, however, that no single characterization of the spatial and temporal variations of clouds and surfaces will suffice to describe the variety of climate regimes on Earth (e.g., Fig. 3). The "local" success of the many proposed techniques suggests that a combination of several such methods may produce more accurate clear scene radiances in global results (Coakley and Baldwin 1984; Rossow et al. 1985; Saunders 1986; Saunders and Kriebel 1988; Minnis et al. 1987). In effect, by performing a series of tests and comparing their results, such a method searches for the best characterization of the radiance variations for each locale. Such a multistep algorithm has been designed for ISCCP (Schiffer and Rossow 1983, 1985).

Although other conventional sources of data may not be directly usable in place of satellite clear scene measurements, they may provide additional information about each location that can help decide which characteristics are most effective for cloud detection in different climate regimes. This second key result is demonstrated by our use of several correlative datasets. We were able to exploit the differences in the land and ocean climates because we employed a dataset that labeled each satellite observation as being over land or water. The use of the vegetation classification of land allowed us to test for the homogeneity of the retrieved surface properties and to remove some cloud contamination. Conventional land surface temperature observations were used to account for synoptic variations.

Use of more such correlative data sets in the cloud detection analysis seems likely to improve results.

The third key result of this study is the illustration of an important additional method of validating the results. Since the cloud detection results depend on the accuracy of the clear scene radiances, which, in turn, depend primarily on the surface properties, a key part of the validation of a satellite cloud climatology can be provided by good surface measurements of reflectance and temperature at 0.6 and 11 μm, where the atmosphere is nearly transparent. This approach avoids the difficulties in defining cloud amount consistently for different observation systems.

The fourth key result is a test of the use of multiple datasets in a single, self-consistent radiative analysis. These extra datasets allow for a substantial reduction in the number of assumptions that are made in the radiative model. This principle can be extended to include the use of other satellite measurements to specify more properties of the surface and clouds (e.g., Susskind et al. 1984; Arking and Childs 1985). For example, the combination of a multispectral imaging radiometer and an atmospheric temperature–humidity profiler on one satellite, as on the current NOAA operational weather satellites, presents the best opportunity to exploit this approach by performing a com-

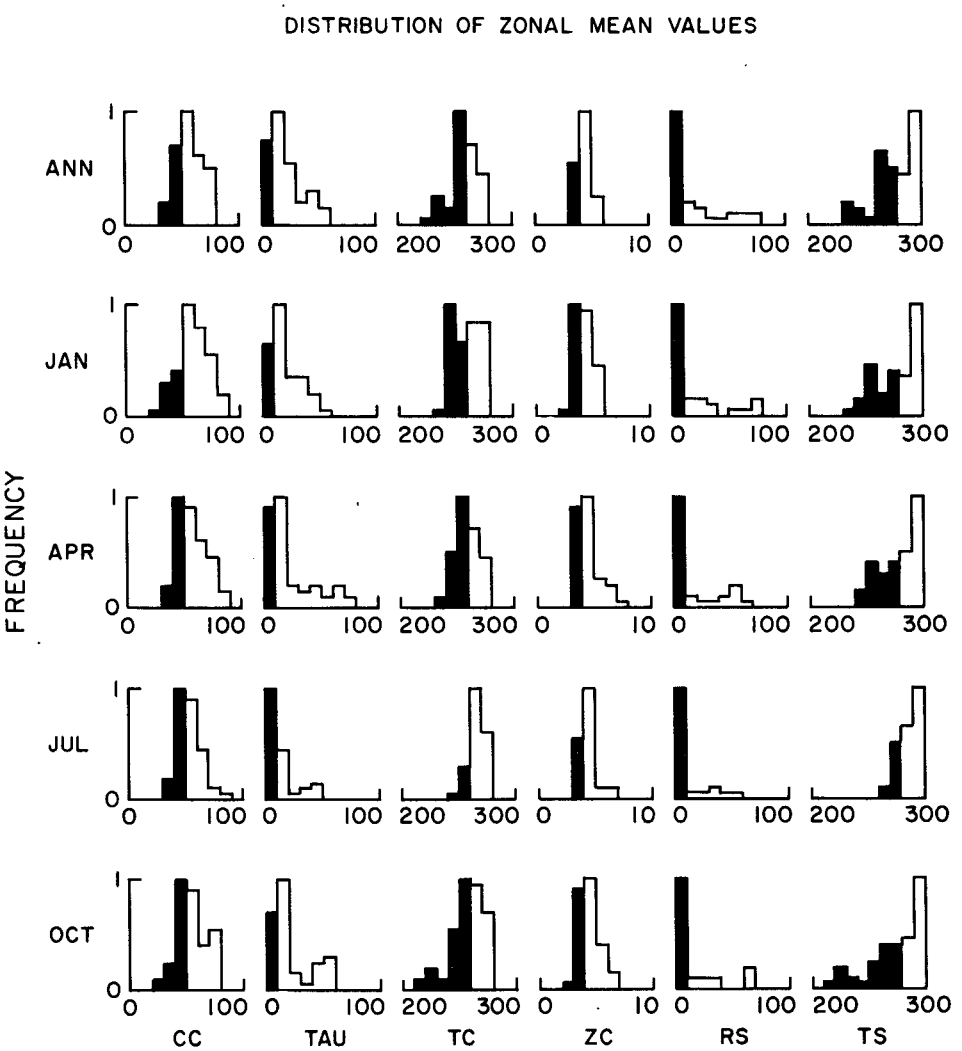

FIG. 12. Distributions of annual and monthly, zonal mean values of cloud amount (CC from 0% to 100%), cloud optical thickness (TAU from 0 to 100), cloud top temperature (TC from 200 to 300 K), cloud top altitude (ZC from 0 to 10 km), surface reflectance (RS from 0% to 100%), and surface temperature (TS from 200 to 300 K). The shading divides each distribution at approximately the annual, global mean value of each parameter.

pletely self-consistent retrieval of surface, cloud, and atmospheric properties from coincident and simultaneous observations. This type of analysis (similar to that performed here or by Susskind et al. 1984, 1987) has not yet been tried using all available spectral channels and instruments, however.

Another advantage of using such multiple datasets and physical models is that the analysis of atmospheric processes with this approach is more comprehensive than is possible using analysis techniques relying on empirical correlations. This approach allows cloud, atmosphere and surface radiative properties to be retrieved separately; thus, their separate contributions to the radiation measured by satellites and to the radiation balance of the climate can be diagnosed. Although the approach could be criticized on the grounds that the models are uncertain, utilizing these models in this type of analysis, together with validation studies at each stage, leads to model improvements—a goal in its own right—that then allow for better remote sensing analyses that overcome this objection. Currently, the accuracy of modeling clear atmospheric effects is limited by the accuracy of the data used to specify the atmospheric temperature and water vapor profiles (Luther 1984), although accurate specification of the continuum absorption coefficient is still a problem. The major limitations in modeling surface radiative effects relate to uncertainties in the angular and spectral dependence of surface radiances (e.g., Koepke and Kriebel 1987); but improved knowledge of these factors can be obtained by further analysis of the available satellite data (see Ro89). The greatest improvements in the cloud properties retrieved from satellite data analysis will come from an improved treatment of the radiative effects of cloud inhomogeneities (cf. Stephens 1988; Rossow 1988). Again, the best source of information about cloud structures over a large range of scales is satellite observations (Cox et al. 1987).

Finally, the value of this kind of analysis of satellite data for climate studies can be illustrated by comparing the estimated uncertainties in the derived parameters (cloud amount, cloud optical thickness, cloud top temperature and altitude, surface reflectance, and surface temperature) with the observed variability of these parameters. Figure 12 shows the distribution of annual and monthly, zonal mean values of these quantities at 1 deg latitudinal resolution; consideration of regional variations would broaden these distributions only slightly. The error assessment presented here demonstrates that these results are accurate enough to resolve these larger-scale variations of clouds and surfaces and are, therefore, valuable to the study of cloud processes in climate.

The measurement of the cloud-radiative feedbacks on the seasonal temperature cycle requires much further work, however (see Part II). Not only are the uncertainties in the cloud property variations still relatively large, but also the conversion of these variations into net radiative flux variations introduces many additional sources of uncertainty. Improving remote sensing analysis models also increases our understanding of the processes that control the radiation balance of earth; this understanding can be incorporated into the simulation of the climate, in particular to improve the flux calculations in climate GCM's.

As stated in the Introduction, there have not been many systematic climatological studies of cloudiness using satellite data, despite the large number of proposed analysis methods. In particular, analyses that provide enough information about the clouds to determine their effects on the total radiation budget are few. Minnis and Harrison (1984a) have pursued a similar strategy to ours, namely, retrieval of cloud and surface properties from narrowband satellite imagery and calculation of the radiation budget implications using these retrieved quantities. Their study focused on determination of the diurnal variability of clouds and their radiative feedbacks at lower latitudes. Our results are complementary to those of Minnis and Harrison in that we have focused on the seasonal variations over the whole globe. Difficulties with the analysis technique and limitations of the data make our polar region results incomplete. The NIMBUS-7 cloud climatology (Hwang et al. 1988; Stowe et al. 1988, 1989) should provide similar, but more extensive, seasonal statistics. The ISCCP cloud climatology will provide a comprehensive examination of diurnal, synoptic, seasonal, and interannual variations of clouds for the whole globe (Schiffer and Rossow 1983).

Acknowledgments. The complexity of this study required many years of effort on the part of many people. Sastri Vemury constructed the first versions of the cloud detection algorithm and conducted early validation studies. Kiyoshi Kawabata and Scott Davis constructed the radiation code and Louis Kanganis carried out the surface temperature comparison study. Kelvin Lee improved and performed additional sensitivity studies of the radiation code and carried out the ocean surface reflectance model and data comparison. Edward Kinsella played an especially key role in compiling and analyzing the production output; all of the cloud analysis statistics presented here were produced by Kinsella, assisted by S. Chan. Discussions with a large number of colleagues during this study helped shape its direction and focus: we thank Albert Arking, James Coakley, Edwin Harrison, Frederick Mosher, Patrick Minnis, Ehrhard Raschke, Genevieve Sèze, Eric Smith, Graeme Stephens, Larry Stowe, Joel Susskind, and Steve Warren. We especially thank Inez Fung, Elaine Matthews, and David Rind for comments on the manuscript. Photographs were created using software written by Jeff Jonas and hardcopy was produced by Patrice Palmer. Graphics were drawn by Lilly

DelValle; final text processing was performed by Elizabeth Devine. Support was provided by the NASA Climate Program managed by Robert Schiffer.

REFERENCES

Alexander, R. C., and R. L. Mobley, 1976: Monthly average sea-surface temperatures and ice-pack limits on a 1° global grid. *Mon. Wea. Rev.*, **104**, 143–148.

Arking, A., 1964: Latitudinal distribution of cloud cover from TIROS III photographs. *Science*, **143**, 569–572.

——, and J. D. Childs, 1985: Retrieval of cloud cover parameters from multispectral satellite measurements. *J. Climate Appl. Meteor.*, **24**, 322–333.

Asano, S., and M. Sato, 1980: Light scattering by randomly oriented spheroidal particles. *Appl. Opt.*, **19**, 962–974.

Barnett, T. P., 1984: Long-term trends in surface temperature over the oceans. *Mon. Wea. Rev.*, **112**, 303–312.

Barry, R. G., A. Henderson-Sellers and K. P. Shine, 1984: Climate sensitivity and the marginal cryosphere. *Climate Processes and Climate Sensitivity*, J. Hansen and T. Takahashi, Eds., *Geophys. Monogr.*, **29**, Amer. Geophys. Union, 221–237.

Barton, I. J., 1983: Dual channel satellite measurements of sea surface temperature. *Quart. J. Roy. Meteor. Soc.*, **109**, 365–378.

——, 1985: Transmission model and ground truth investigation of satellite-derived sea surface temperatures. *J. Climate Appl. Meteor.*, **24**, 508–516.

Berlyand, T. G., and L. A. Strokina, 1980: Zonal cloud distribution on the Earth. *Meteor. Gidrol.*, **3**, 15–23.

Bernstein, R. L., 1982: Sea surface temperature estimation using the NOAA-6 satellite Advanced Very High Resolution Radiometer. *J. Geophys. Res.*, **87**, 9455–9465.

Bowman, K. P., and A. J. Krueger, 1985: A global climatology of total ozone from the Nimbus 7 Total Ozone Mapping Spectrometer. *J. Geophys. Res.*, **90**, 7967–7976.

Bunting, J. T., and R. F. Fournier, 1980: Tests of spectral cloud classification using DMSP fine mode satellite data. AFGL-TR-80-0181, Environ. Res. Papers, No. 704, U.S. Air Force Geophysics Laboratory, Hanscom AFB, 42 pp.

Carroll, J. J., and B. W. Fitch, 1981: Effects of solar elevation and cloudiness on snow albedo at the South Pole. *J. Geophys. Res.*, **86**, 5271–5276.

Cess, R. D., 1976: Climate change: An appraisal of atmospheric feedback mechanisms employing zonal climatology. *J. Atmos. Sci.*, **33**, 1831–1843.

——, B. P. Briegleb and M. S. Lian, 1982: Low-latitude cloudiness and climate feedback: Comparative estimates from satellite data. *J. Atmos. Sci.*, **39**, 53–59.

Chahine, M. T., 1974: Remote sounding of cloudy atmospheres. Part I: The single cloud layer. *J. Atmos. Sci.*, **31**, 233–243.

——, 1977: Remote sounding of cloudy atmospheres. Part II: Multiple cloud formations. *J. Atmos. Sci.*, **34**, 744–757.

——, 1982: Remote sensing of cloud parameters. *J. Atmos. Sci.*, **39**, 159–170.

——, H. H. Aumann and F. W. Taylor, 1977: Remote sensing of cloudy atmospheres. Part III: Experimental verifications. *J. Atmos. Sci.*, **34**, 758–765.

Chou, M.-D., J. Childs and P. Dorian, 1986: Cloud cover estimation using bispectral satellite measurements. *J. Climate Appl. Meteor.*, **25**, 1280–1292.

Coakley, J. A., 1987: A dynamic threshold method for obtaining cloud cover from satellite imagery data. *J. Geophys. Res.*, **92**, 3985–3990.

——, and F. P. Bretherton, 1982: Cloud cover from high-resolution scanner data: Detecting and allowing for partially filled fields of view. *J. Geophys. Res.*, **87**, 4917–4932.

——, and D. G. Baldwin, 1984: Towards the objective analysis of clouds from satellite imagery. *J. Climate Appl. Meteor.*, **23**, 1065–1099.

Cohen, S. G. Ed., Oxford World Atlas, 1973, Oxford University Press, 190 pp.

Conlan, E. F., 1973: Operational products from ITOS scanning radiometer data. NOAA Tech. Rep., NESS 52, U.S. Dept. of Commerce, Washington, DC, 57 pp.

Cox, C., and W. Munk, 1956: Slopes of the sea surface deduced from photographs of the sun glitter. *Bull. Scripps Inst. Oceanogr.*, **6**, 401–488.

Cox, S. K., D. S. McDougal, D. A. Randall and R. A. Schiffer, 1987: FIRE—The First ISCCP Regional Experiment. *Bull. Amer. Meteor. Soc.*, **68**, 114–118.

Curran, R. J., R. Wexler and M. L. Nack, 1978: Albedo climatology analysis and the determination of fractional cloud cover. NASA Tech. Memo. 79576, NASA Goddard Space Flight Center, Greenbelt, MD, 45 pp.

Cutten, D. R., 1985: Atmospheric broadband transmission measurements and predictions in the 8–13 μm window: Influence of water continuum absorption errors. *Appl. Opt.*, **24**, 1085–1087.

Davies, R., 1978: The effect of finite geometry on the three-dimensional transfer of solar irradiance in clouds. *J. Atmos. Sci.*, **35**, 1712–1725.

——, 1984: Reflected solar radiances from broken cloud scenes and the interpretation of scanner measurements. *J. Geophys. Res.*, **89**, 1259–1266.

d'Entremont, R. P., 1986: Low- and midlevel cloud analysis using nighttime multispectral imagery. *J. Climate Appl. Meteor.*, **25**, 1853–1869.

Desbois, M., and G. Sèze, 1984: Use of space and time sampling to produce representative satellite cloud classifications. *Ann. Geophys.*, **2**(5), 599–606.

——, —— and G. Szejwach, 1982: Automatic classification of clouds on METEOSAT imagery: Application to high-level clouds. *J. Appl. Meteor.*, **21**, 401–412.

Duggin, M. J., 1985: Factors limiting the discrimination and quantification of terrestrial features using remotely sensed radiance. *Int. J. Remote Sensing*, **6**, 3–27.

Duvel, J. P., and R. S. Kandel, 1984: Anisotropy of longwave radiation emergent from a broken cloud field and its effect on satellite estimates of flux. *J. Climate Appl. Meteor.*, **23**, 1411–1420.

Ellingson, R. G., 1982: On the effects of cumulus dimensions on longwave irradiance and heating rate calculations. *J. Atmos. Sci.*, **39**, 886–896.

England, C. F., and G. E. Hunt, 1985: A bispectral method for the automatic determination of parameters for use in imaging satellite cloud retrievals. *Int. J. Remote Sensing*, **6**, 1545–1553.

Fortuna, J. F., and L. N. Hambrick, 1974: The operation of the NOAA polar satellite system. NOAA Tech. Memo. NESS 60, U.S. Dept. of Commerce, Washington, DC, 127 pp.

Fye, F. K., 1978: The AFGWC Automated Cloud Analysis Model. Tech Memo. 78-002, USAF, Offut AFB, Nebraska, 97 pp.

GARP, 1975: *The Physical Basis of Climate and Climate Modeling.* GARP Publ. Ser. No. 16, World Meteorological Organization, 265 pp.

——, 1978: GARP Climate Dynamics Sub-programme. *JOC Study Conference on Parameterization of Extended Cloudiness and Radiation for Climate Models*, Oxford, England, World Meteorological Organization, 37 pp.

Gates, W. L., and A. B. Nelson, 1975: A new (revised) tabulation of the Scripps topography on a 1° global grid. Part I: Terrain heights. Rep. R-1276-1-ARPA, Rand Corp., Santa Monica, 132 pp.

Grassl, H., 1974: Influence of different absorbers in the window region on radiative cooling (and on surface temperature determination). *Beit. Phys. Atmos.*, **47**, 1–13.

Grenfell, T. C., and G. A. Maykut, 1977: The optical properties of ice and snow in the Arctic basin. *J. Glaciol.*, **18**, 445–463.

Gruber, A., 1977: Determination of the Earth-atmosphere radiation budget from NOAA satellite data. NOAA Tech. Rep., NESS 76, U.S. Dept. of Commerce, Washington, DC, 28 pp.

Gutman, G., D. Tarpley and G. Ohring, 1987: Cloud screening for determination of land surface characteristics in a reduced resolution satellite data set. *Int. J. Remote Sensing,* **8,** 859–870.

Hale, G. M., and M. R. Querry, 1973: Optical constants of water in the 200-nm to 200-μm wavelength region. *Appl. Opt.,* **12,** 555–563.

Hansen, J. E., and L. D. Travis, 1974: Light scattering in planetary atmospheres. *Space Sci. Rev.,* **16,** 527–610.

——, G. Russell, D. Rind, P. Stone, A. Lacis, L. Travis, S. Lebedeff and R. Ruedy, 1983: Efficient three-dimensional global models for climate studies: Models I and II. *Mon. Wea. Rev.,* **111,** 609–662.

——, A. Lacis, D. Rind, G. Russell, P. Stone, I. Fung, R. Ruedy and J. Lerner, 1984: Climate sensitivity: Analysis of feedback mechanisms. *Climate Processes and Climate Sensitivity,* Geophys. Monogr., **29,** Amer. Geophys. Union, 130–163.

Harris, R., and E. C. Barrett, 1978: Toward an objective nephanalysis. *J. Appl. Meteor.,* **17,** 1258–1266.

Harshvardhan, and J. A. Weinman, 1982a: Infrared radiative transfer through a regular array of cuboidal clouds. *J. Atmos. Sci.,* **39,** 431–439.

——, and ——, 1982b: Solar reflection from a regular array of horizontally-infinite clouds. *Appl. Opt.,* **21,** 2940–2944.

——, and R. Thomas, 1984: Solar reflection from interacting and shadowing cloud elements. *J. Geophys. Res.,* **89,** 7179–7185.

Hartmann, D. L., and D. A. Short, 1980: On the use of earth radiation budget statistics for studies of clouds and climate. *J. Atmos. Sci.,* **37,** 1233–1250.

Henderson-Sellers, A., 1986: Layer cloud amounts for January and July 1979 from 3D-nephanalysis. *J. Climate Appl. Meteor.,* **25,** 118–132.

——, and N. A. Hughes, 1985: 1979 3D-nephanalysis global total cloud amount climatology. *Bull. Amer. Meteor. Soc.,* **66,** 626–627.

Hilsenrath, E., and B. M. Schlesinger, 1981: Total ozone seasonal and interannual variations derived from the 7 year NIMBUS-4 BUV data set. *J. Geophys. Res.,* **86,** 12 087–12 096.

——, D. F. Heath and B. M. Schlesinger, 1979: Seasonal and interannual variations in total ozone revealed by the NIMBUS-4 Backscattered Ultraviolet Experiment. *J. Geophys. Res.,* **84,** 6969–6979.

Holben, B., and R. S. Fraser, 1984: Red and near-infrared sensor response to off-nadir viewing. *Int. J. Remote Sensing,* **5,** 145–160.

Hughes, N. A., 1984: Global cloud climatologies: A historical review. *J. Climate Appl. Meteor.,* **23,** 724–751.

——, and A. Henderson-Sellers, 1985: Global 3D-nephanalysis of total cloud amount: Climatology for 1979. *J. Climate Appl. Meteor.,* **24,** 669–686.

Hummel, J. R., and R. A. Reck, 1979: A global surface albedo model. *J. Appl. Meteor.,* **18,** 239–253.

Hwang, P. H., L. L. Stowe, H. Y. M. Yeh, H. L. Kyle and NIMBUS-7 Cloud Data Processing Team, 1988: The NIMBUS-7 global cloud climatology. *Bull. Amer. Meteor. Soc.,* **69,** 743–752.

Inn, E. C. Y., and Y. Tanaka, 1953: Absorption coefficient of ozone in the ultraviolet and visible regions. *J. Opt. Soc. Amer.,* **43,** 870–873.

Inoue, T., 1987: A cloud type classification with NOAA-7 split-window measurements. *J. Geophys. Res.,* **92,** 3991–4000.

Jacobowitz, H., and A. Gruber, 1975: Calibration of the visible channel of the NOAA 2 scanning radiometer. *Abstracts, Second Conference on Atmospheric Radiation,* Arlington, VA, Amer. Meteor. Soc., 67.

Jasperson, W. H., and G. D. Nastrom, 1984: A comparison of NMC and GWC analysis field temperatures with aircraft measurements. *J. Climate Appl. Meteor.,* **23,** 1421–1426.

Kimes, D. S., 1983: Dynamics of directional reflectance factor distributions for vegetation canopies. *Appl. Opt.,* **22,** 1364–1372.

Kistler, R. E., and D. F. Parrish, 1982: Evolution of the NMC data assimilation system: September 1978–January 1982. *Mon. Wea. Rev.,* **110,** 1335–1346.

Koepke, P., and K. T. Kriebel, 1987: Improvements in the shortwave cloud-free radiation budget accuracy. Part I: Numerical study including surface anisotropy. *J. Climate Appl. Meteor.,* **26,** 374–395.

Koffler, R., A. G. DeCotiis and P. Krishna Rao, 1973: A procedure for estimating cloud amount and height from satellite infrared radiation data. *Mon. Wea. Rev.,* **101,** 240–243.

Kondratyev, K. Ya., 1969: *Radiation in the Atmosphere.* International Geophysics Series, Vol. 12, Academic Press, 912 pp.

——, 1973: *Radiation Characteristics of the Atmosphere and the Earth's Surface.* Amerind Pub. Co., 580 pp.

Kuhn, M., and L. Siogas, 1978: Spectroscopic studies at McMurdo, South Pole, and Siple stations during the austral summer 1977–78. *Antarctic J. U.S.,* **13,** 178–179.

Lacis, A. A., and J. E. Hansen, 1974: A parameterization for the absorption of solar radiation in the Earth's atmosphere. *J. Atmos. Sci.,* **31,** 118–133.

Lamb, H. H., 1972: *Climate: Present, Past and Future.* Fundamentals and Climate Now, Vol. I, Methuen, 613 pp.

Llewellyn-Jones, D. T., P. J. Minnett, R. W. Saunders and A. M. Zavody, 1984: Satellite multichannel infrared measurements of sea surface temperature of the N.E. Atlantic Ocean using AVHRR/2. *Quart. J. Roy. Meteor. Soc.,* **110,** 613–631.

London, J., 1957: A study of atmospheric heat balance. Final Report, Contract AF19(122)-165, AFCRC-TR-57-287, College of Engineering, New York University, NY, 99 pp.

——, R. D. Bojkov, S. Oltmans and J. I. Kelly, 1976: Atlas of the global distribution of total ozone, July 1957–June 1967. NCAR Tech. Note, 113 + STR, National Center for Atmospheric Research, Boulder, CO, 276 pp.

Luther, F. M., 1984: The Intercomparison of Radiation Codes in Climate Models, Longwave Clear-sky Calculations. World Climate Research Programme, WCP-93, World Meteorological Organization, 37 pp.

Masaki, G. T., 1976: The Wolf Plotting and Contouring Package. GSFC Computer Program Lib. #A00227, Computer Sciences Corporation, Goddard Space Flight Center, Greenbelt, MD, 187 pp.

Matthews, E., 1983: Global vegetation and land use: New high resolution data bases for climate studies. *J. Climate Appl. Meteor.,* **22,** 474–487.

——, 1985: Atlas of archived vegetation, land-use and seasonal albedo data bases. NASA Tech. Memo. 86199, 53 pp.

——, and W. B. Rossow, 1987: Regional and seasonal variations of surface reflectance from satellite observations at 0.6 μm. *J. Climate Appl. Meteor.,* **26,** 170–202.

Maul, G., 1981: Application of GOES visible-infrared data to quantifying mesoscale ocean surface temperature. *J. Geophys. Res.,* **86,** 8007–8021.

——, and M. Sidran, 1973: Atmospheric effects on ocean surface temperature sensing from NOAA satellite scanning radiometer. *J. Geophys. Res.,* **78,** 1909–1916.

——, P. W. de Witt, A. Yanaway and S. R. Baig, 1978: Geostationary satellite observations of Gulf Stream meanders: Infrared measurements and time series analysis. *J. Geophys. Res.,* **83,** 6123–6135.

McClain, E. P., W. G. Pichel and C. C. Walton, 1985: Comparative performance of AVHRR-based multichannel sea surface temperatures. *J. Geophys. Res.,* **90,** 11 587–11 601.

McCleese, D. J., and L. S. Wilson, 1976: Cloud top height from temperature sounding instruments. *Quart. J. Roy. Meteor. Soc.,* **102,** 781–790.

McKee, T. B., and S. K. Cox, 1974: Scattering of visible radiation by finite clouds. *J. Atmos. Sci.,* **31,** 1885–1892.

——, M. DeMaria, J. A. Kuenning and S. K. Cox, 1983: Comparison of Monte Carlo calculations with observations of light scattering in finite clouds. *J. Atmos. Sci.,* **40,** 1016–1023.

McMillin, L. M., and C. Dean, 1982: Evaluation of a new operational technique for producing clear radiances. *J. Appl. Meteor.*, **21**, 1005–1014.

McPherson, R. D., K. H. Bergman, R. E. Kistler, G. E. Rasch and D. S. Gordon, 1979: The NMC operational global data assimilation system. *Mon. Wea. Rev.*, **107**, 1445–1461.

Miller, D. B., and R. G. Feddes, 1971: Global Atlas of Relative Cloud Cover. US National Environmental Satellite Service and USAF Environmental Technical Applications Center, AD 739434-Rep. No. 1, Washington, DC, 140 pp.

Minnis, P., and E. F. Harrison, 1984a: Diurnal variability of regional cloud and clear sky radiative parameters derived from GOES data. Part I: Analysis method. *J. Climate Appl. Meteor.*, **23**, 993–1011.

——, and ——, 1984b: Diurnal variability of regional cloud and clear sky radiative parameters derived from GOES data. Part II: November 1978 cloud distributions. *J. Climate Appl. Meteor.*, **23**, 1012–1031.

——, and ——, 1984c: Diurnal variability of regional cloud and clear sky radiative parameters derived from GOES data. Part III: November 1978 radiative parameters. *J. Climate Appl. Meteor.*, **23**, 1032–1051.

——, —— and G. G. Gibson, 1987: Cloud cover over the equatorial eastern Pacific derived from July 1983 International Satellite Cloud Climatology Project data using a hybrid bispectral threshold method. *J. Geophys. Res.*, **92**, 4051–4074.

Miyakoda, K., and A. Rosati, 1982: The variation of sea surface temperature in 1976 and 1977. Part 1: Data analysis. *J. Geophys. Res.*, **87**, 5667–5680.

Naber, P. S., and J. A. Weinman, 1984: The angular distribution of infrared radiances emerging from broken fields of cumulus clouds. *J. Geophys. Res.*, **89**, 1249–1257.

Njoku, E. G., 1985: Satellite-derived sea surface temperature: Workshop comparisons. *Bull. Amer. Meteor. Soc.*, **66**, 274–281.

NOAA, 1977a: Environmental Satellite Imagery, January, April, July, October 1977. NOAA/NESS Environmental Data Service, National Oceanic and Atmospheric Administration, U.S. Dept. of Commerce, Washington, DC.

——, 1977b: Northern Hemisphere Average Snow and Ice Boundaries, 3 January 1977 through 2 January 1978. NOAA/NESS Synoptic Analysis Section, National Oceanic and Atmospheric Administration, U.S. Dept. of Commerce, Washington, DC.

——, 1984: Oceanographic Monthly Summary: Eastern–Western Arctic Sea Ice Edge Climatology. J. Wartha-Clark, Ed. National Oceanic and Atmospheric Administration, U.S. Department of Commerce, Washington, DC, 52 pp.

Ohring, G., and P. Clapp, 1980: The effect of changes in cloud amount on the net radiation at the top of the atmosphere. *J. Atmos. Sci.*, **37**, 447–454.

Parkinson, C. L., J. C. Comiso, H. J. Zwally, D. J. Cavalieri, P. Gloerson and W. J. Campbell, 1987: Arctic Sea Ice, 1973–1976: Satellite Passive-Microwave Observations. NASA SP-489, National Aeronautics and Space Administration, Washington, DC, 296 pp.

Payne, R. E., 1972: Albedo of the sea surface. *J. Atmos. Sci.*, **29**, 959–970.

Phillips, N., L. McMillin, A. Gruber and D. Wark, 1979: An evaluation of early operational temperature soundings from TIROS-N. *Bull. Amer. Meteor. Soc.*, **60**, 1188–1197.

Phulpin, T., M. Derrien and A. Brard, 1983: A two-dimensional histogram procedure to analyse cloud cover from NOAA satellite high resolution imagery. *J. Climate Appl. Meteor.*, **22**, 1332–1345.

Pinty, B., and G. Szejwach, 1985: A new technique for inferring surface albedo from satellite observations. *J. Climate Appl. Meteor.*, **24**, 741–750.

Platt, C. M. R., 1979: Remote sounding of high clouds. Part I: Calculations of visible and infrared optical properties from lidar and radiometer measurements. *J. Appl. Meteor.*, **18**, 1130–1143.

——, and G. L. Stephens, 1980: The interpretation of remotely sensed high cloud emittances. *J. Atmos. Sci.*, **37**, 2314–2322.

——, and A. C. Dilly, 1981: Remote sounding of high clouds. Part IV: Observed temperature variations in cirrus optical properties. *J. Atmos. Sci.*, **38**, 1069–1082.

——, D. W. Reynolds and N. L. Abshire, 1980: Satellite and lidar observations of the albedo, emittance and optical depth of cirrus compared to model calculations. *Mon. Wea. Rev.*, **108**, 195–204.

Posey, J. W., and P. F. Clapp, 1964: Global distribution of normal surface albedo. *Geofis. Int.*, **4**, 33–48.

Prabhakara, C., and G. Dalu, 1976: Remote sensing of the surface emissivity at 9 μm over the globe. *J. Geophys. Res.*, **81**, 3719–3724.

Reynolds, D. W., and T. H. Vonder Haar, 1977: A bi-spectral method for cloud parameter determination. *Mon. Wea. Rev.*, **105**, 446–457.

Reynolds, R. W., 1983: A comparison of sea surface temperature climatologies. *J. Climate Appl. Meteor.*, **22**, 447–459.

Roberts, R. E., J. E. A. Selby and L. M. Biberman, 1976: Infrared continuum absorption by atmospheric water vapor in the 8–12 μm window. *Appl. Opt.*, **15**, 2085–2090.

Robock, A., and D. Kaiser, 1985: Satellite-observed reflectance of snow and clouds. *Mon. Wea. Rev.*, **113**, 2023–2029.

Rosen, R. D., and D. A. Salstein, 1980: A comparison between circulation statistics computed from conventional data and NMC Hough analyses. *Mon. Wea. Rev.*, **108**, 1226–1247.

Rossow, W. B., Ed., 1981: Clouds in Climate: Modeling and Satellite Observational Studies. Report of workshop held at NASA Goddard Institute for Space Studies, New York, 222 pp.

——, 1989: Measuring cloud properties from space: A review. *J. Climate*, **2**, 201–213.

——, E. Kinsella and L. Garder, 1983: Seasonal and global cloud variations deduced from polar orbiting satellite radiance measurements. *Proc. Fifth Conference on Atmospheric Radiation*, Baltimore, MD, Amer. Meteor. Soc., 195–198.

——, F. Mosher, E. Kinsella, A. Arking, M. Desbois, E. Harrison, P. Minnis, E. Ruprecht, G. Sèze, C. Simmer and E. Smith, 1985: ISCCP cloud algorithm intercomparison. *J. Climate Appl. Meteor.*, **24**, 877–903.

——, C. L. Brest and L. C. Garder, 1989: Global, seasonal surface variations from satellite radiance measurements. *J. Climate*, **2**, 214–247.

——, A. A. Lacis and P.-J. Lu, 1990: Global, seasonal cloud and radiation budget variations from satellite radiance measurements. Part 2: Results. *J. Climate* (in preparation).

Ruff, I., and A. Gruber, 1975: Graphical relations between a satellite and a point viewed perpendicular to the satellite velocity vector (side scan). NOAA Tech. Memo., NESS 65, U.S. Dept. of Commerce, Washington, DC, 14 pp.

Sakellariou, N. K., and H. G. Leighton, 1988: Identification of cloud-free pixels in inhomogeneous surfaces from AVHRR radiances. *J. Geophys. Res.*, **93**, 5287–5293.

Sato, Ma., K. Kawabata and J. E. Hansen, 1977: A fast invariant imbedding method for multiple scattering calculations and an application to equivalent widths of CO_2 lines on Venus. *Astrophys. J.*, **216**, 947–962.

Saunders, R. W., 1985: Monthly mean cloudiness observed from METEOSAT-2. *J. Climate Appl. Meteor.*, **23**, 114–127.

——, 1986: An automated scheme for the removal of cloud contamination from AVHRR radiances over western Europe. *Int. J. Remote Sensing*, **7**, 867–886.

——, and K. T. Kriebel, 1988: An improved method for detecting clear sky and cloudy radiances from AVHRR data. *Int. J. Remote Sensing*, **9**, 123–150.

Scharfen, G., R. G. Barry, D. A. Robinson, G. Kukla and M. C. Serrize, 1987: Large-scale patterns of snow melt on Arctic sea ice mapped from meteorological satellite imagery. *Ann. Glaciol.*, **9**, 1–6.

Schiffer, R. A., and W. B. Rossow, 1983: The International Satellite Cloud Climatology Project (ISCCP): The first project of the World Climate Research Program. *Bull. Amer. Meteor. Soc.*, **64,** 779–784.

——, and ——, 1985: ISCCP global radiance data set: A new resource for climate research. *Bull. Amer. Meteor. Soc.*, **66,** 1498–1505.

Schmetz, J., 1984: On the parameterization of the radiative properties of broken clouds. *Tellus*, **36A,** 417–432.

Schutz, C., and W. L. Gates, 1971a: Global climatic data for surface, 800 mb and 400 mb: January. Rep. for Advanced Research Projects Agency, RAND, R-915-ARPA, Santa Monica, CA, 21 pp.

——, and ——, 1971b: Global climatic data for surface, 800 mb and 400 mb: July. Rep. for Advanced Research Projects Agency, RAND, R-1029-ARPA, Santa Monica, CA, 22 pp.

Sèze, G., and M. Desbois, 1987: Cloud cover analysis from satellite imagery using spatial and temporal characteristics of the data. *J. Climate Appl. Meteor.*, **26,** 287–303.

——, and W. B. Rossow, 1989: Time-cumulated visible and infrared radiance histograms used as descriptors of surface and cloud variations. *J. Climate* (submitted).

Shenk, W. F., and V. V. Salomonson, 1972a: A simulation study exploring the effects of sensor spatial resolution on estimates of cloud cover from satellites. *J. Appl. Meteor.*, **12,** 214–220.

——, and ——, 1972b: A multispectral technique to determine sea surface temperature using NIMBUS 2 data. *J. Phys. Oceanogr.*, **2,** 157–167.

——, and R. J. Curran, 1973: A multi-spectral method of estimating cirrus cloud top heights. *J. Appl. Meteor.*, **12,** 1213–1216.

——, R. J. Holub and R. A. Neff, 1976: A multispectral cloud type identification method developed for tropical ocean areas with NIMBUS 3 MIRR measurements. *Mon. Wea. Rev.*, **104,** 284–291.

Simmer, C., E. Raschke and E. Ruprecht, 1982: A method for determination of cloud properties from two-dimensional histograms. *Ann. Meteor.*, **18,** 130–132.

Smith, W. L., H. M. Woolf, C. M. Hayden, D. Q. Wark and L. M. McMillin, 1979: The TIROS-N Operational Vertical Sounder. *Bull. Amer. Meteor. Soc.*, **60,** 117–118.

Somerville, R. C. J., and L. A. Remer, 1984: Cloud optical thickness feedbacks in the CO2 climate problem. *J. Geophys. Res.*, **89,** 9668–9672.

Stamm, A. J., and T. H. Vonder Haar, 1970: A study of cloud distributions using reflected radiance measurements from the ATS satellites. *J. Appl. Meteor.*, **9,** 498–507.

Stephens, G. L., 1980: Radiative transfer on a linear lattice: Application to anisotropic ice crystal clouds. *J. Atmos. Sci.*, **37,** 2095–2104.

——, 1988: Radiative transfer through randomly fluctuating optical media. Part II: Group theory. *J. Atmos. Sci.*, **45,** 1837–1848.

——, and P. J. Webster, 1981: Clouds and climate: Sensitivity of simple systems. *J. Atmos. Sci.*, **38,** 235–247.

Stowe, L. L., 1984: Evaluation of NIMBUS 7 THIR/CLE and Air Force three-dimensional nephanalysis estimates of cloud amount. *J. Geophys. Res.*, **89,** 5370–5380.

——, C. G. Wellemeyer, T. F. Eck, H. Y. M. Yeh and NIMBUS-7 Cloud Data Processing Team, 1988: NIMBUS-7 global cloud climatology. Part I: Algorithms and validations. *J. Climate,* **1,** 445–470.

——, H. Y. M. Yeh, T. F. Eck, C. G. Wellemeyer and NIMBUS-7 Cloud Data Processing Team, 1989: NIMBUS-7 global cloud climatology. Part II: First year results. *J. Climate* (in press).

Streten, N. A., and D. J. Pike, 1980: Characteristics of the broadscale Antarctic sea ice extent and the associated atmospheric circulation 1972–1977. *Arch. Meteor. Geophys. Bioklim.*, **29,** 279–299.

Susskind, J., J. Rosenfield, D. Reuter and M. T. Chahine, 1984: Remote sensing of weather and climate parameters from HIRS2/MSU on TIROS-N. *J. Geophys. Res.*, **89,** 4677–4697.

——, D. Reuter and M. T. Chahine, 1987: Cloud fields retrieved from analysis of HIRS2/MSU sounding data. *J. Geophys. Res.*, **92,** 4035–4050.

Takashima, T., and Y. Takayama, 1981: Emissivity and reflectance of the model sea surface for the use of AVHRR data of NOAA satellites. *Pap. Meteor. Geophys.*, **32,** 267–274.

Telegadas, K., and J. London, 1954: A physical model of the Northern Hemisphere troposphere for Winter and Summer. Sci. Rep. No. 1, AF19(122)-165, New York University, 55 pp.

Toon, O. B., and J. B. Pollack, 1976: A global average model of atmospheric aerosols for radiative transfer calculations. *J. Appl. Meteor.*, **15,** 225–246.

Van Loon, H., 1972: Cloudiness and precipitation in the Southern Hemisphere. *Meteorology of the Southern Hemisphere, Meteor. Monogr.* No. 13, C. W. Newton, Ed., 101–104.

Vonder Haar, T. H., 1970: Application of simultaneous infrared radiation measurements and cloud photographs from satellites. *J. Appl. Meteor.*, **9,** 955–958.

Wadhams, P., 1981: The ice cover in the Greenland and Norwegian seas. *Rev. Geophys. Space Phys.*, **19,** 345–393.

Wang, W-C., W. B. Rossow, M-S. Yao and M. Wolfson, 1981: Climate sensitivity of a one-dimensional radiative-convective model with cloud feedback. *J. Atmos. Sci.*, **38,** 1167–1178.

Warren, S. G., 1982: Optical properties of snow. *Rev. Geophys. Space Phys.*, **20,** 67–89.

——, and E. P. Shettle, 1986: Optical constants of ice in the infrared atmospheric windows. Preprints, *Sixth Conference on Atmospheric Radiation,* Williamsburg, Amer. Meteor. Soc., 103–105.

——, C. J. Hahn and J. London, 1985: Simultaneous occurrence of different cloud types. *J. Climate Appl. Meteor.*, **24,** 658–667.

WCRP, 1984: Scientific Plan for the World Climate Research Programme. WCRP Publ. Series, No. 2, WMO/TD—No. 6, World Meteorological Organization, 95 pp.

Welch, R. M., and B. A. Wielicki, 1984: Stratocumulus cloud field reflected fluxes: The effect of cloud shape. *J. Atmos. Sci.*, **41,** 3085–3103.

Wright, P., 1986: Problems in the use of ship observations for the study of interdecadal climate changes. *Mon. Wea. Rev.*, **114,** 1028–1034.

Yamanouchi, T., 1983: Variations of incident solar flux and snow albedo on the solar zenith angle and cloud cover, at Mizuho Station, Antarctica. *J. Meteor. Soc. Jpn.*, **61,** 879–893.

——, K. Suzuki and S. Kawaguchi, 1987: Detection of clouds in Antarctica from infrared multispectral data of AVHRR. *J. Meteor. Soc. Jpn.*, **65,** 949–962.

Yeh, H. Y., 1984: Determination of cloud parameters from infrared sounder data. *J. Geophys. Res.*, **89,** 11 759–11 770.

——, T. H. Vonder Haar and K-N. Liou, 1985: Cloud parameters and temperature profile retrieval from infrared sounder data. *J. Atmos. Sci.*, **42,** 2360–2370.

Young, M. J., 1967: Variability in estimating total cloud cover from satellite pictures. *J. Appl. Meteor.*, **6,** 573–579.

Zwally, H. J., J. C. Comiso, C. L. Parkinson, W. J. Campbell, F. D. Corsey and P. Gloersen, 1983: Antarctic Sea Ice, 1973–1976: Satellite Passive-Microwave Observations. NASA SP-459, National Aeronautics and Space Administration, Washington, DC, 206 pp.